© Copyright 2020

Koichiro Tanaka

Interface Engineering to Enhance the Mechanical Performance of Aluminum Thin Film Deposited on PET Substrate

Koichiro Tanaka

A thesis submitted in partial fulfillment of the requirements for the degree of

Master of Science

University of Washington

2020

Reading Committee:

Professor Junlan Wang, Chair

Professor Dwayne Arola, Co-chair

Program Authorized to Offer Degree:

Department of Materials Science and Engineering

University of Washington

Abstract

Interface Engineering to Enhance the Mechanical Performance of Aluminum Thin Film Deposited on PET Substrate

Koichiro Tanaka

Chair of Supervisory Committee:
Professor Junlan Wang
Department of Mechanical Engineering

Al films magnetron sputtered on PET substrates with varying interfacial adhesion were produced by controlling the time of the plasma etching prior to the Al deposition. Uniaxial tension and laser-induced thin film spallation tests were performed on the Al film and PET substrate to investigate the effect of the adhesion on the ductility of the Al film. In addition, the effect of substrate thickness was studied using substrates with varying thicknesses. The laser spallation measurement revealed that the adhesion between the Al film and PET substrate increased from less than 5.3 MPa to 37 MPa by applying 10 min-plasma etching. The surface analysis indicated the chemical state of the surface is the dominant factor for the improved interfacial adhesion.

The uniaxial tensile test of the PET supported Al film showed that the failure strain of Al film was improved by applying the plasma etching. It is assumed that the shear stress caused by the mismatch in the strain of Al and PET leads to local delamination of the Al film. When the plasma etching was applied, the interfacial adhesion was considered to increase strong enough to prevent the delamination. Accordingly, the PET substrate retarded the strain concentration in Al film by constraining the deformation of Al film, leading to an increase in the failure strain of Al film.

The failure strain of Al film with 50 µm-thick PET substrate was substantially lower than the Al film with 12, and 25 µm-thick PET. According to the shear lag theory, the shear stress at the interface increases with an increase in the load acting on the PET substrate. Thus, it is considered that the shear stress was high enough to cause the delamination of Al film even the interfacial adhesion increased with the plasma etching.

The Al film deposited on 25µm-thick PET showed the maximum failure strain when the plasma etching time was 5 min. The result of the contact angle measurement indicated the effect of the chemical modification reaches constant when the plasma etching time was more than 5 min. On the other hand, the line surface profile indicated the plasma etching might form a periodic swell on the surface of the PET, and the swell appeared to become sharp as the plasma etching time increased. It is possible that the swell decreased the failure strain of the Al film by initiating the stress concentration during the tensile test. Due to the combination of the two effects, the failure strain of the Al film exhibited the maximum value when the plasma etching time was 5 min.

Table of Contents

List of Figures

List of Tables

ACKNOWLEDGEMENTS

First and foremost, I want to express my sincere gratitude to my two academic advisors, Professor Junlan Wang and Professor Dwayne D. Arola, for their encouragement, patience, and guidance on my research and graduate study. Their advice is invaluable not only for my academic research but also for my future career development. I want to thank my labmates, Melicent Stossel and Yang Zhou, for their strong support in the experiments. Most of the work would not have been possible without their kindness, patience, and knowledge. I would also like to express my thanks to Dr. Brian Flinn, Alex Gray, for the help on using the equipment for contact angle measurements; staff in Molecular Analysis Facility, Dr. Micah Glaz, and Scott Braswell, for the surface analysis; Dr. Hanson Fong for the help and training on using SEM; all members of our research group for many discussions, which kept me motivated and gave me ideas from different points of views. I want to acknowledge the financial support from JX Nippon Mining and Metals Corporation and the Applied Master's Program at the University of Washington for my graduate study. Finally, I would like to thank my family and friends for their love and support.

Chapter 1. Introduction

1. 1 Motivation

A combination of metallic films and polymeric materials have long been utilized for various kinds of industrial products, such as circuit boards and integrated circuits, because of their unique properties that combine a high conductivity of metals and a good insulating capability of polymeric materials. Recently, growing attention is being paid on metal films deposited on flexible polymer substrates as a core material of deformable electronics, including thin-film transducers [1], flexible solar cells [2], and wearable devices [3]. The metal films for these applications are required to be ductile in order to tolerate deformations resulting from the manufacturing process and consumer use. This demand necessitates, and has led to, a large number of studies about the mechanical performance of polymer-supported metal films.

In general, free-standing metal films subjected to a uniaxial tensile strain easily fail at a few percent of strain [4] [5]. In contrast, it has been demonstrated that metal films supported by polymer substrates show much higher ductility than free-standing metal films. The fundamental mechanism of the improvement in ductility is that the polymer substrate constrains the deformation of the metal film and retards a local thinning [6] [7]. On the other hand, it has also been reported that the various kinds of factors in the metal-polymer system influence the improvement mechanism.

However, the influence of some of these factors such as the interfacial adhesion, and the substrate thickness, have not been fully understood. Besides, most of the studies only focus on a particular factor by eliminating the influence of the other factors, leading to the lack of broad perspective which is required to design the whole system.

The primary purpose of this study is to understand the improving mechanism of polymer-supported metal films, and to further enhance the ductility of the metal films. Although a wide range of systems including multilayer metal films deposited on polymer substrates [8], fatigue property of the films under cyclic loading [9], and biaxial stress state of the films [10] have been studied, the most simple structure and stress state (i.e. a single layer of metal films supported by a polymer substrate under the uniaxial tensile strain) is the focus of this study, which aims to increase our understanding of the mechanism.

1. 2 Literature Review

In this section, a literature review on the affecting properties of metal-polymer laminates on thin metal film ductility was performed, in order to grasp the recent progress in this research field and propose the direction of the research. This review indicated several properties that directly influence ductility.

1. 2. 1 Thickness of Metal Films

The thickness of the metal films largely influences the ductility of metal films. N. Lu et al. discussed the effect of the thickness of the metal films on the failure strain of metal-polymer composite by conducting a uniaxial tensile test of Cu films with a thickness of 50 nm to 1000 nm deposited on 12 μm-thick polyimide (PI) films. They demonstrated that Cu films with a thickness less than 100nm behave in a brittle manner due to dimensional constraints on dislocation activity, resulting in a grain boundary decohesion at a smaller strain. Cu film with a thickness from 200 nm to 1 μm showed a ductile trans-granular fracture, and the failure strain reached a maximum of more than 50 % when the thickness of the Cu film was 500 nm [11]. Besides, R. M. Niu et al. reported the same trend of thickness dependence of Cu films, using materials with a thickness range from 60 to 700 nm deposited on PI substrates. The authors concluded that thinner Cu film had a lower failure strain due to constraining effect on dislocation mobility [12].

On the other hand, Z. H. Cao and co-workers demonstrated that the stretchability of Cu film deposited on PI substrate decreased with increasing thickness of Cu film from 70 to 600 nm [13] [14]. According to the authors, the residual stress in Cu films became higher in thicker Cu film because Cu film was not annealed after sputtering deposition, causing the debonding of Cu film from the substrate at smaller strains [14].

Even though these studies discussed the same system of Cu films deposited on PI substrates, and the thickness of Cu films was within the same range, the trend in ductility of Cu films with respect to the thickness did not agree. The experimental details of these studies are listed in Table 1.1. The comparison indicates that the microstructure of the Cu films (annealing vs. as deposited), and the adhesion between Cu films and PI substrates (with vs. without plasma etching) are the possible causes of the discrepancy.

Table 1.1. Experimental details for Cu/PI system in literature

PI h_s (μm)	Cu h_f (nm)	Annealing	Plasma Etching	Trend in Ductility	Literature
12.7	50 to 1000	150°C×1h	Yes	improved with increasing h_f	[11]
125	60 to 700	100°C×2h	Yes	improved with increasing h_f	[12]
125	70 to 600	No	No	improved with decreasing h_f	[14]
125	40 to 600	No	No	improved with decreasing h_f	[13]

1. 2. 2 Microstructure of Metal Films

In addition to the thickness, the microstructure of the metal films such as grain size also influences the ductility of the metal films. N. Lu et al. experimentally demonstrated that annealed Cu films deposited on PI substrates were able to be elongated more than 25% without any cracks, even though cracks were initiated at a 12% strain in non-annealed Cu films supported by the same PI substrates. As concluded in this study, the cause of the difference seems to be that the applied tensile load inhibits uniformity in grain size by stimulating particular grains to grow, leading to strain localization [15]. The rearrangement and growth of Al grains assisted by the tensile stress were observed and supported by the other literature [16].

In addition to the grain size, the orientation of the grains in metal films influences the ductility of the metal films. The finite element analysis of a Cu film supported by a PI substrate revealed that a small portion of (100) grains in Cu films surrounded by (111) grains act the role of soft inclusion leading to strain localization because (100) grains are softer than (111) grains [11].

Therefore, grains in the metal films should be fully grown to prevent the partial growth of the grains assisted by the tensile strain energy, which leads to the strain concentration. Thus, uniformity and orientation are also essential for metal films to be ductile.

1. 2. 3 Substrate

Although no literature has specifically focused on this line of inquiry, the effect of substrates can be implied from some literature. For instance, different failure strains of Cu film have been reported, i.e., 8 % [12] vs. 24 % [11] for 340 nm-thick Cu films, even though these Cu films have been fabricated using almost the same procedure except for the thickness of the PI substrate as shown in Table 1.1. Another example was that silver (Ag) film deposited on a poly-ethylene terephthalate (PET) substrate tolerated a higher strain than the same Ag film deposited on a PI substrate [17]. Moreover, M. Chen et al. claimed, based on their investigation of the failure strains of Ag, Al and Cu films deposited on PET substrate, that the mismatch of Young's modulus and Poisson's ratio between metal films and polymer substrates may influence the ductility of the metal films [18]. These studies indicate the thickness of the substrates influences the ductility of the metal films. Furthermore, the proportion of the metal films and polymer substrates with respect to the thickness and mechanical properties should be emphasized as a contributor to ductility, rather than solely the thickness of the metal films.

On the other hand, it should be noted that the examples mentioned above could also indicate the effect of the adhesion because the adhesions of metal films in this literature are probably different from each other, and not quantitatively measured. Since measuring the adhesion between thin metal films and polymer substrates is challenging as discussed in 1. 2. 5, there has been no literature separately discussing the effect of adhesion and the other factors.

1. 2. 4 Strain Rate

It has been reported that the failure strain of metal films increased with increasing strain rate for the system of Al films supported by PET substrates [19], and Cu films supported by PI substrates [14]. Z. H. Cao et al. discussed that Young's modulus of the PI substrate increased with increasing strain rate due to the viscoelastic characteristic while Young's modulus of the Cu film was insensitive to strain rate. Therefore, Dundur' parameter, α (*), decreased with increasing strain rate, leading to a decrease in the toughness of Cu films, which relates to $1/(1-\alpha)$ [14].

(*) $\alpha = (\bar{E}_f - \bar{E}_s)/(\bar{E}_f + \bar{E}_s)$, where $\bar{E}_f = E_f/(1-\nu_f^2)$, and $\bar{E}_s = E_s/(1-\nu_s^2)$. E is Young's modulus and ν is Poisson's ration. The subscript of f, and s represent film, and substrate, respectively

1. 2. 5 Adhesion of Metal Films

The adhesion between metal films and polymer substrates is one of the most important factors influencing the ductility of the polymer-supported metal films. The well-known way to increase the adhesion is to add a bonding layer, such as Cr and Ti. Adding a bonding layer between the Cu film and PI substrate improved the ductility of the Cu film by increasing its adhesive strength to the substrate [20]. However, the bonding layer forms cracks at small strain, since it is brittle in general. The cracks in the bonding layer induce cracks in the film deposited on the bonding layer due to stress concentration [21]. Due to the inefficacy of this method, another promising approach to improve the adhesion is to coat a primer that provides the surface of a polymer substrate with a thin chemical layer making strong bonds to the deposited metal film. For example, the failure strain of Ag film deposited on a PET substrate improved by coating primer on the surface of the PET prior to the deposition [17]. Moreover, the bond between a primer coating layer and a metal film can be strengthened by the elevating temperature, leading to a further increase in the ductility of the metal film [22]. The other common way to improve adhesion is a plasma treatment. Some of the literature discussed in a former section [11] [15] utilized the plasma treatment to obtain a well-bonded metal-polymer sample. A plasma treatment will be discussed in section 1. 2. 7.

In these studies, the adhesive strength was evaluated qualitatively, rather than quantifying the numerical value of adhesion, by comparing the appearance of samples with different fabricating conditions after the peeling test. Obtaining a specific value of interfacial adhesion is, in general, challenging for common adhesion measurement methods [23] [24]. Thus, no literature has quantitatively discussed the effect of the adhesion on the ductility of metal films.

1. 2. 6 Laser Spallation

Laser-induced thin film spallation technique causes a debonding of a thin film from a substrate with stress waves induced by a high-power pulse laser. The common adhesion measurement methods such as scratch, peel, pull, blister, and indentation test, tend to be qualitative and comparable due to the complex stress state caused by a large plastic deformation during the test. By contrast, the laser spallation technique can achieve quantitative results [25]. For example, the interfacial adhesions of Zeolite fabricated with three different methods on the Si substrate were successfully measured, and the influence of the fabrication methods on the interfacial adhesion was qualitatively discussed [26].

Recently, some studies have tried to apply this technique to polymer films. The interfacial strength of the poly-*p*-phenylene-benzobisoxazole (PBO) and silicon nitride was determined by the laser spallation technique to reveal the effect of processing conditions and surface roughness [27]. The adhesive strength between PI films and Si substrates with three different interlayers: silicon nitride, silicon oxynitride, silicon oxide was measured with the laser spallation test [28]. There has been no literature trying to apply this technique to a multilayer system with polymer substrates. However, the laser spallation technique may be ideal for the metal-polymer system because the significantly high strain rate (~10^7/s) associated with the high-magnitude stress wave is expected to minimize the influence of the viscoelastic behavior of polymer substrate.

1. 2. 7 Plasma Etching

Plasma treatment is widely utilized for metalized polymers to improve adhesion between metal films and polymer substrates. When a small amount of gaseous material such as Ar, N_2, and O_2 is subjected to the strong electric field under a high vacuum environment, gas atoms or molecules are decomposed into gas ions and electrons (e.g., $\mathrm{Ar} \rightarrow \mathrm{Ar}^+ + \mathrm{e}^-$). Then the positively charged gas ions are accelerated by the electric field and collide with the gas atoms or molecules, producing more gas ions. When the process continuously occurs, the state is called “plasma,” and plasma treatment is the surface treatment utilizing the plasma.

For the case of Ar plasma treatment onto the surface of PET, Ar ions bombard the surface of the PET and break C-O, C=O, C-C, and C-H bonds [29]. The debonding leaves free radicals of C, H, and O on the surface, and the radicals form the cross-linking on the surface of PET [30]. The plasma treatment increases the wettability of the PET surface against the polar liquid [31], leading to the increase in surface free energy (SFE) due to the formation of cross-linkings [30] [32]. In addition, it is indicated that adhesion of PET surface increases with an increase in SFE [33]. Although appropriate conditions for the plasma treatment to maximize the SFE have been suggested in the studies mentioned above, the conditions such as gas pressure, plasma power, and treatment time should be optimized for our treatment systems and materials.

1. 3 Research Direction

The metal-PI and metal-PET systems mentioned in this section are summarized in Table 1.2 and Table 1.3, respectively. The effect of the microstructure has been well studied. The metal films consisting of well oriented and fully grown grains are desirable to achieve high ductility. Heat treatment will be a practical and effective way to obtain the desired microstructure. The influence of the strain rate on the ductility of the metal films has also been verified. The appropriate strain rate for this study should be found at first so that the consistent rate is employed for all experiments. By contrast, most of the studies discussing the metal thickness dependence have not paid attention to the effect of the substrates, resulting in a lack of understanding about the role of proportion in film ductility. The proportion of the thickness and mechanical properties such as Young's modulus and Poisson's ratio will also influence the ductility of the polymer-supported metal films in addition to the thickness of metal films. Thus, there is still room for further improvement in ductility of metal films from the point of view of the congruity of metal films and polymer substrates. In addition, the effect of the adhesion has been discussed only qualitatively, even though a lot of studies have pointed out that good adhesion is essential to improve the ductility of the metal film. This is because of the difficulty of the adhesion measurement as discussed, and the laser spallation technique could be the solution to the problem. Plasma etching is an effective way to modify the surface of a polymer substrate and increase the adhesion of a metal film to a polymer substrate. If the operating conditions such as power, gas pressure, and treatment time are optimized for our system, metal/polymer laminates with different adhesion can be produced.

Based on the literature review, the primary purpose of this study is to investigate the effect of adhesion between metal films and substrates on the ductility of the metal film. Particularly, metal/polymer samples with various adhesive strength are produced by applying the plasma etching. Then the adhesion of the samples is measured with the laser spallation technique, and its effect on the ductility of the metal films is quantitatively discussed. Moreover, the effect of the proportion of the metal films and the substrates is discussed by using substrates with varying thicknesses.

It is expected that there is a critical proportion to enhance the ductility of the metal film. Understanding the proportion will help to determine the suitable polymer material for a certain metal film, and vice versa. Moreover, the proportion will be able to motivate the development of metal and polymer materials for flexible electronics by providing desirable mechanical properties. I believe this will be a big contribution to the advancement in flexible electronics.

The metal film used in this study is aluminum (Al) which is one of the common metals for thin film conductors because of its high conductivity and cost-effectiveness [19]. PET is used as a substrate because it is a promising polymer material for flexible electronics because of its superior transparency, mechanical properties, and affordable prices [17] [34].

Table 1.2. Summary of the literature review for metal films supported by PI substrates

Polymer Substrate		Metal Film		Annealing	Surface Treatment	Testing Conditions		Factor(s) improving ductility	Literature
polymer	thickness, h_s (μm)	metal	thickness, h_f (μm)			strain rate (sec^{-1})	sample shape and size		
PI	12.7	Cu	50, 100, 200, 350, 500, 1000	150°C×1h	Plasma Etching	3.3×10^{-4}	rectangular 5mm×30mm	increasing h_f	[11]
PI	125	Cu	60, 100, 275, 340, 700	100°C×2h	Plasma Etching	1.0×10^{-4}	dogbone 4mm×20mm	increasing h_f	[12]
PI	125	Cu	70, 200, 400, 600	no	no	1.0×10^{-5} to 5.0×10^{-2}	dogbone 4mm×20mm	decreasing h_f	[14]
PI	125	Cu	40, 70, 200, 600	no	no	8.3×10^{-3}	dogbone 4mm×20mm	decreasing h_f	[13]
PI	12.7	Cu	1000	no / 200°C×0.5h	Plasma Etching	3.3×10^{-4}	rectangular 5mm×30mm	annealing	[15]
PI	12.7	Cu	1000	200°C×0.5h	10nm Cr interlayer	3.3×10^{-4}	rectangular 5mm×30mm	Cr bonding layer	[20]
PI	12.7	Ag	380, 600	no / 250°C×2h	no	3.12×10^{-4}	rectangular 1mm×16mm	annealing, and thicker metal film	[17]

Table 1.3. Summary of the literature review for metal films supported by PET substrates

Polymer Substrate		Metal Film		Annealing	Surface Treatment	Testing Conditions		Factor(s) improving ductility	Litera-ture
polymer	thickness, h_s (μm)	metal	thickness, h_f (μm)			strain rate (sec^{-1})	sample shape and size		
PET	12	Ag	380, 600	no	primer coating	3.12×10^{-4}	rectangular 1mm×16mm	primer coating	[17]
PET	50	Ag, Cu, Al	3000, 6700, 12000, 20000	no	no	6.67×10^{-4}	rectangular 10mm×50mm	increasing h_f for Cu	[18]
PET	127	Al	50, 100, 200, 500	no	no	1.67×10^{-3} to 1.67×10^{-2}	rectangular 13mm×160mm	decreasing h_f	[19]
PET	12	Ag	200	no	primer coating	1×10^{-4}	rectangular 1mm×28mm	elevated temperature	[22]

Chapter 2. Experimental Details

2. 1 Sputtering Deposition

PET sheet with thickness of 12, 25, 50 and 450 μm (Toray Plastics America, Inc. by courtesy, Lumirror U65) were used as the substrate. The PET substrates were cut into a specific shape for each test before sputtering depositions. The sputtering depositions were performed with the magnetron sputtering system (AJA International Inc. Model Orion5-UHV dual DC magnetron sputtering system). The substrates were ultrasonically cleaned with isopropyl alcohol for 15 minutes before they were installed into the sputtering chamber. After installation, the chamber was vacuumed down to a pressure less than 3×10^{-6} Torr. The plasma etching with an RF power of 28 W was applied to the surface of the substrates prior to the sputtering deposition. The Ar gas pressure during the etching was 4 mTorr, and the etching time was 1, 3, 5, or 10 minutes. Al thin films were deposited on the substrates rotating at 20 rpm. The sputtering was performed by using an Al target with a purity of 99.999 % at a rate of 3.3 nm/min with 100 W DC power. The Ar gas pressure during the sputtering was 4 mTorr.

2. 2 Tensile Testing

2. 2. 1 Sample Preparation

The PETs were cut into a rectangular or a dog-bone shape. For rectangular samples, the PETs were cut into shape with a width of 5 mm and a length of 25 mm using a razor blade. The specially designed ruler shown in Figure 2.1 was used for the cutting to make the two long sides of the rectangular exactly parallel. For dog-bone samples, the PETs were pressed using a hand pressing tool and the dog-bone shape mold. The tool, mold, and dimensions of the pressed samples are shown in Figure 2.2. The tensile direction was parallel to the machine direction of PET sheets for all of the samples regardless of the shape of the sample. After cutting, Al films with a thickness of 50 and 500nm were deposited on the PETs following the procedure described in section 2. 1.

Figure 2.1. The ruler for rectangular shape cutting

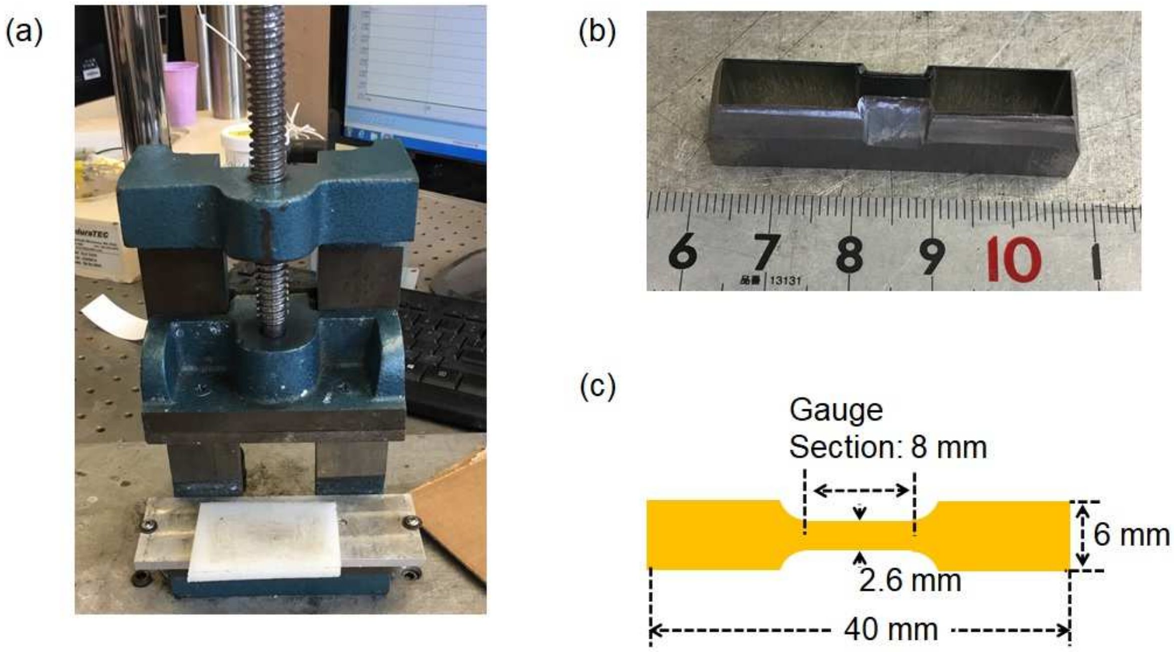

Figure 2.2. Stamping tools for dog-bone shape sample. (a) hand stamping tool (b) dog-bone shape mold (c) dimension of the dog-bone samples

2. 2. 2 *Testing Conditions and Setup*

Tensile tests were conducted at a constant strain rate of $1.0 \times 10^{-4}, 1.0 \times 10^{-3}, 1.25 \times 10^{-3}$, and $1.0 \times 10^{-2}\ \mathrm{s}^{-1}$ using the custom-made tensile tester with a resolution of 1 mN and 1 μm. The distance between grip sections was 20 mm for rectangular samples, and 35mm for dog-bone samples. During the tensile tests, the electrical resistance of the Al films was monitored with a digital-multimeter (DMM, Agilent Technologies Inc. Model 34401A) in a four-probe method, and the resistance data were collected using a commercial software (Keysight Technologies Inc.

BenchVue). The schematic of the resistance measurement setup is shown in Figure 2.3. Al foils with the size of 100 mm × 50mm and thickness of 0.017 mm were fold into the size of 10 mm ×25 mm to be gripped together with the sample. The probes from DMM were clipped to the Al foils to avoid direct clipping to the sample, which may influence the result of tensile tests. The gripping parts were covered with Kapton tape to electrically insulate the tensile test equipment from the Al foils, sample, and probes.

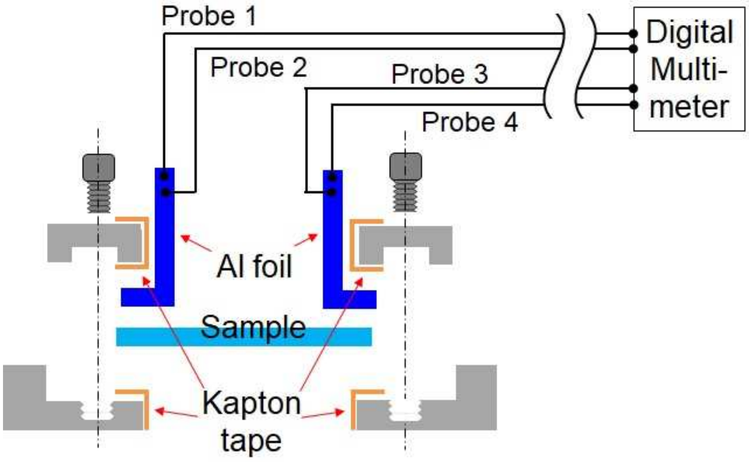

Figure 2.3. Schematic of the resistance measurement setup.

Electrical Resistance Change

The initial resistance, R_0, of the thin film can be described as follows.

$$R_0 = \rho \frac{l_0}{s_0} \tag{2.1}$$

where ρ is the resistivity of the metal film, l_0 is the length of the specimen, and s_0 is the cross-section of the metal film.

When the tensile load is applied to the specimen, the length increases to l_1, and the cross-section of the specimen decreases to s_1 due to the shrinkage in width and thickness resulting from Poisson's effect. Assuming the volume of the specimen does not change, the cross-section, s_1 can be described as:

$$l_1 = l_0 + \Delta l \tag{2.2}$$

$$s_1 = \frac{l_0 \cdot s_0}{l_1} \tag{2.3}$$

Then the resistance of the specimen, R_1 can be described as follows by using equation (1) and (3):

$$R_1 = \rho \frac{l_1}{s_1} = \rho \frac{{l_1}^2}{s_0 \cdot l_0} = R_0 \frac{{l_1}^2}{{l_0}^2} \tag{2.4}$$

Substituting equation (2), equation (4) can be rewritten as follows:

$$R_1 = R_0 \left(\frac{l_0 + \Delta l}{l_0} \right)^2 = R_0 (1 + \varepsilon)^2 \tag{2.5}$$

where ε is the engineering strain defined as:

$$\varepsilon = \frac{\Delta l}{l_0}$$

Equation (2.5) indicates that the resistance of the specimen is expected to increase as the applied strain increases. Thus, the deviation of measured resistance from this expected relation indicates non-uniform deformation of the metal film such as local thinning, and cracking.

2. 2. 3 Digital Image Correlation

Digital image correlation (DIC) technique was employed to measure the displacement data obtained from the tensile testing system. Black sprinkles were evenly painted using a black ink spray (Rust-Oleum Co. Ultra Cover 2X, Flat Black) as a pattern for the imaging on the surface of the rectangular Al/PET specimen prepared with a procedure described in 2. 2. 1. Before making the sprinkles, a white base painting was coated onto the surface with a white ink spray (Rust-Oleum Co. Ultra Cover 2X, White Primer) to enhance the contrast of the sprinkles. The specimen was elongated with the tensile testing system to a displacement of 20 mm at a strain rate of 1.25×10^{-3} sec^{-1}, and the photographs of the surface were recorded every second with a high-resolution digital camera (IDS Imaging Development Systems GmbH. Model UI-3180CP-M-GL) and a focal camera lens (CBC America LLC. Model Computar TV lens 50mm). 100 to 120 images out of 800 images were evenly extracted for each sample, and the strain for each image was analyzed and calculated using a software.

2. 3 Laser Spallation Test

2. 3. 1 Sample Preparation

The layered structure of the samples for laser spallation tests is shown in Figure 2.4. The structure (a) is the basic structure for the test, and the structure (b) is used to modify the shape of the stress wave [25]. The role of each layer is described in the next section.

2. 3. 1. 1 Sample (a)

The PET substrates were cut into a circle with a diameter of 1” using scissors. An Al film with a thickness of 600 or 1000 nm was deposited on one side of the PET as the test film. Another 400 nm-thick Al film was deposited on the other side of the PET as the energy absorbing layer. The sputtering depositions of the test films and absorbing layers were conducted by following the procedure detailed in section 2. 1. After the deposition, water glass (The Science Co., Sodium Silicate Liquid, technical grade) was coated by the spin coating system (Laurell Technologies Co., Model WS-400BZ-6NPP Lite) onto the absorbing layer as the confining layer. The rotation speed and time of the spin coating was 2000 rpm and 5 min, respectively. The thickness of the water glass layer was around 10 μm.

2. 3. 1. 2 Sample (b)

The Al test film with a thickness of 600, or 1000 nm, was deposited on one side of the PET substrate. Aside from that, the Al energy absorbing layer 400 nm-thick Al film was deposited on the SiO_2 disc (Quartz Scientific Inc., quartz polished disc) with a diameter of 1” and thickness of 1/8”, 1/16”, or 1/44”. The un-sputtered sides of the PET and the SiO_2 disc were adhered together by water glass (the same one for confining layer), or super glue (Henkel Co., Duro super glue adhesive). The following procedures were employed for the bonding to obtain a thin and uniform adhesive layer, and to prevent containing air bubbles in the adhesion layer. A water glass confining layer was then spin-coated onto the absorbing layer.

2. 3. 1. 3 Bonding procedure

<u>450 μm-thick PET sample</u>

The PET substrates were cut into a 1”-diameter circle, and Al test film was deposited. A drop of water glass or super glue was applied onto the center of the un-sputtered side of SiO_2 disc, and then the PET substrate was placed on top and pressed with a finger. After removing the excess adhesive squeezed out of the interface, the sample was sandwiched with glass slides and clamped with a staples-binder-clip for for at least 12 hours.

12-50 μm-thick PET sample

The PET substrates were cut into 60 × 60 mm squares, and Al test film was deposited. A drop of super glue or water glass was applied onto the un-sputtered side of PET, and then the SiO_2 disc was placed on top and pressed with a finger. After removing the excess adhesive squeezed out of the interface, the pressure of approximately 300 g/cm^2 was kept applying onto the SiO_2 using a binder clip for at least 12 hours. Finally, the PET squares were trimmed into 1”-diameter circle.

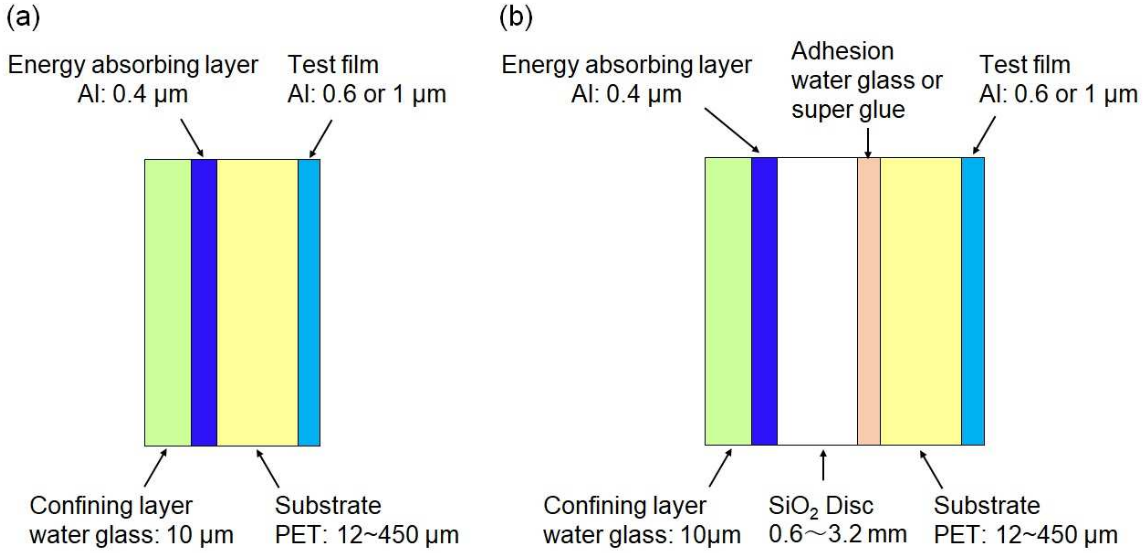

Figure 2.4. The layer structure of the samples for the laser spallation test (a) the basic layer structure, (b) The structure added SiO_2 to modify the shape of the stress wave.

2. 3. 2 Experimental procedure

The experimental setup of the laser spallation is schematically illustrated in Figure 2.5. The system consists of two sides. One side is the pulsing laser system, which induces a laser to create a stress wave for a spallation. The other side is the probing system, so-called Michaelson interferometer, which is designed to monitor the high-speed displacement at the surface caused by the laser-induced stress-wave loading.

A 5 ns Nd: YAG pulse laser with a wavelength of 1064 nm was focused into 1 to 2 mm-diameter on the absorbing layer of the sample. The varying energy ranging from 30 to 270 mJ was employed. The Al layer absorbs the laser energy and undergoes a sudden expansion. Since the Al layer is confined between the water glass layer and the substrate, the sudden expansion produces a compressive stress wave toward the surface of the sample. After reaching the free surface, the compressive stress wave reflects back into the tensile wave.

At the same time, out-of-plane displacement of the loaded surface was monitored by the probing system. 10-20 mW linearly polarized argon-ion laser with 514 nm in wavelength was used as the probing light. The argon ion laser is split into two beams at the beam splitter. One beam is directed to the mirror, and the other beam is directed to the surface of the sample. The two beams are reflected back and recombined at the beam splitter. Since the laser reflected from the surface changes in phase due to the displacement of the surface, the two lasers interfere with each other. The interference signals were detected by the photodetector and digitized by a 5 GHz oscilloscope (Teledyne Technologies (LeCroy) Inc., Model Wavemaster 8500) at a sampling rate of 0.05 ns per point (or 20G Sample/second). The displacement can be determined by analyzing the interference signals.

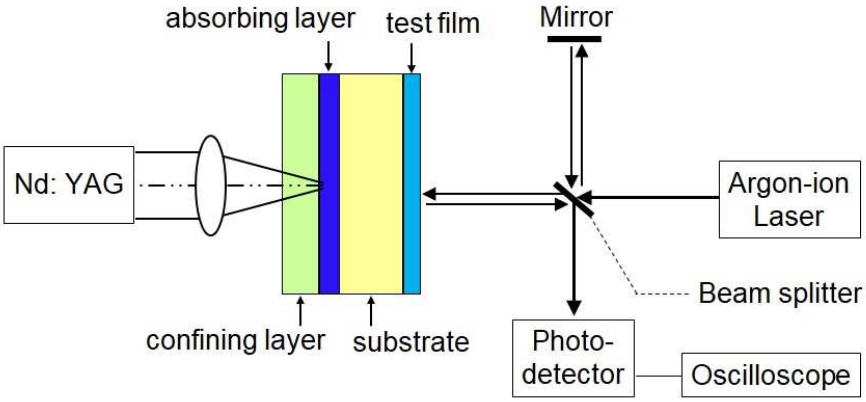

Figure 2.5. Schematic illustration of the laser spallation testing setup.

2. 3. 3 Measuring principles

When the pulsed laser is impinged on the specimen, stress wave oscillates the free surface of the specimen. The vibration of the surface makes a phase shift by changing the light path (i. e., the distance from the beam splitter to the surface of the specimen). As a result, the two lasers interfere with each other due to the difference in phase when they are recombined at the beam splitter. The velocity of the vibration surface, $V(t)$, can be described using the fringe frequency of the interference laser light, ν_0, as [35]:

$$V(t) = \frac{1}{2}\lambda_0 \nu_0(t), \tag{2.6}$$

where λ_0 is the wavelength of the probing laser.

By integrating the equation, the displacement history, $u(t)$, is obtained in terms of the fringe count of the interference fringes, $n(t)$, as:

$$u(t) = \frac{1}{2}\lambda_0 n(t). \tag{2.7}$$

On the other hand, the intensity of the interference laser detected at the photodetector can be described in terms of the fringe count as:

$$I(t) = \frac{I_{max} + I_{min}}{2} + \frac{I_{max} - I_{min}}{2}\sin(2\pi n(t) + \varphi) \tag{2.8}$$

where I_{max} and I_{min} are the maximum and minimum intensities of the interference fringes, and φ is the phase angle. Substituting the fringe count obtained from the Eq. (2.8) into Eq. (2.7), the displacement history of the free surface can be calculated.

The substrate stress, σ_{sub}, and the interface, σ_{int}, caused by the laser-induced stress wave can be determined from the displacement history using the principle of one-dimensional wave mechanics as:

$$\sigma_{sub}(t) = -\frac{1}{4}(\rho c)_{sub}\frac{\partial}{\partial t}\left\{u\left(t-\frac{h_{film}}{c_{film}}\right)+u\left(t+\frac{h_{film}}{c_{film}}\right)\right\} + \frac{1}{4}(\rho c)_{film}\frac{\partial}{\partial t}\left\{u\left(t-\frac{h_{film}}{c_{film}}\right)-u\left(t+\frac{h_{film}}{c_{film}}\right)\right\} \qquad (2.9)$$

$$\sigma_{int}(t) = -\frac{1}{2}(\rho c)_{film}\frac{\partial}{\partial t}\left\{u\left(t-\frac{h_{film}}{c_{film}}\right)-u\left(t+\frac{h_{film}}{c_{film}}\right)\right\} \qquad (2.10)$$

where ρ, c, and h denote the density, longitudinal wave speed, and thickness, respectively. The subscription sub, film, and int represent the substrate, film, and interface, respectively. For the system with the small film thickness, Eq. (2.9) and (2.10) can be reduced to as follows:

$$\sigma_{sub} = -\frac{1}{2}(\rho c)_{sub}\frac{\partial u}{\partial t}, \qquad (2.11)$$

$$\sigma_{int} = -(\rho h)_{film}\frac{\partial^2 u}{\partial t^2}. \qquad (2.12)$$

Thus, the stress at the substrate and interface can be determined from the displacement of the free surface using Eq. (2.11) and (2.12). The material properties used in this calculation are shown in Table 2.1. The varying pulse laser energy gives a range of σ_{int}, and the σ_{int} needed to spall the Al film can be considered as the adhesive strength of the interface.

Table 2.1. Material properties [36]

Material	Density, ρ [kg/cm^3]	Wave speed, c [m/sec]
PET	1380	1950
Al	2700	6320
SiO_2	2650	5800

2. 4 Sample Analysis

2. 4. 1 SEM observation

The surface of the specimen before and after the tensile or spallation tests were observed with Scanning Electron Microscope (Thermo Fisher Scientific Inc., Model Apreo-S). The SEM images were obtained with an accelerating voltage of 2 kV and a working distance of 8.2 to 8.8 mm.

2. 4. 2 AFM analysis

The surface of the PET substrate before and after applying the plasma etching were examined with Atomic Force Microscopy (AFM, Burker Corp. Model Dimension ICON). The topographic images of 10 μm × 10 μm area were recorded, and the scanning data were analyzed to calculate the surface roughness.

2. 4. 3 Profilometry

The surface profile of the spallation spots was examined with the profilometer (Bruker, Model DektakXT). The height of the spots was scanned with a line scan mode, and a scanning distance was 2 mm.

2. 4. 4 Contact angle measurement

The contact angles of water on the surface of the PET substrate before and after applying the plasma etching were measured with a goniometer (AST PRODUCTS Inc. Model VCA optima). A DI water droplet with a volume of 1 μl was dropped on to the surface of the sample, and the angle was measured using the image captured at 5 sec after the drop. The average value was determined from 5 measurements.

Chapter 3. Results

3. 1 Tensile behavior of the aluminum films deposited on PET substrate

3. 1. 1 PET substrate

Effect of the strain rate and the shape of the sample

Figure 3.1 shows the stress-strain response when the dog-bone and rectangular shape of 25 μm-thick PET were elongated with various strain rates. The tests with a strain rate of 10×10^{-4} sec^{-1} were aborted at a strain of 0.1 due to the limit of the data acquisition. Other tests were conducted until the specimen ruptured. The strain rate did not significantly influence the tensile behavior of the PET substrate. However, yield strength increased with increasing strain rate. This trend agrees well with a general characteristic that polymer materials behave in a brittle manner with a high strain rate.

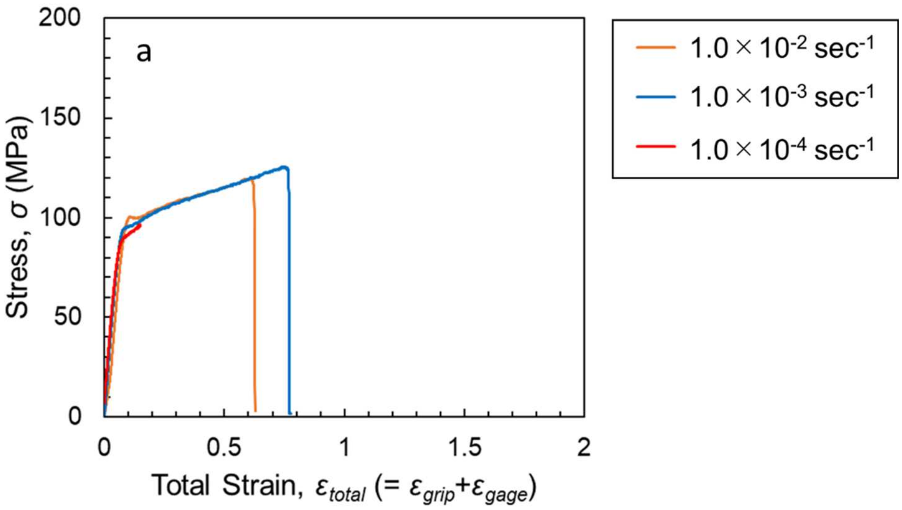

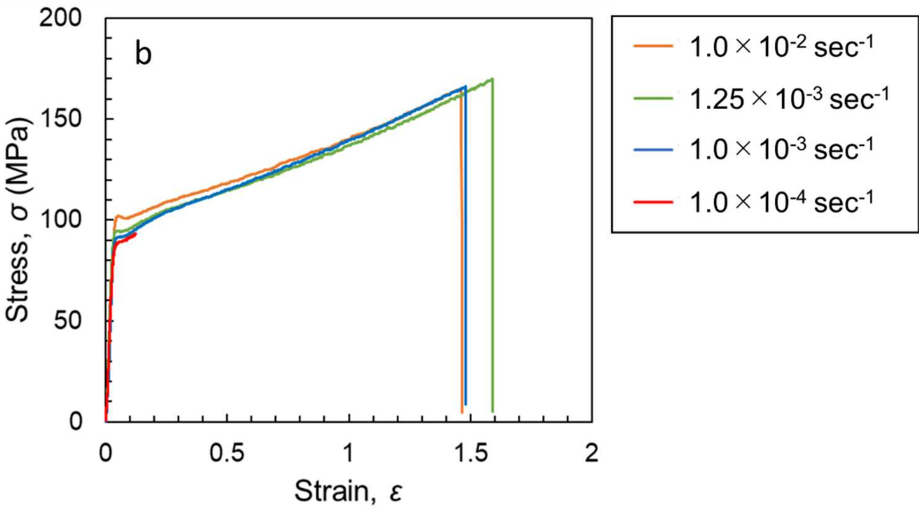

Figure 3.1 Stress strain relationship of 25 μm-thick PET with a shape of a) dog-bone and b) rectangular.

The failure strain of dog-bone and rectangular shape 25 μm-thick PET are summarized and plotted with respect to the strain rate in Figure 3.2. The influence of the strain rate on the failure strain was unclear because the deviation among the sample was more significant than the variation due to the strain rate. On the other hand, the failure strain of the rectangular samples was obviously higher than that of the dog-bone sample, regardless of the strain rate.

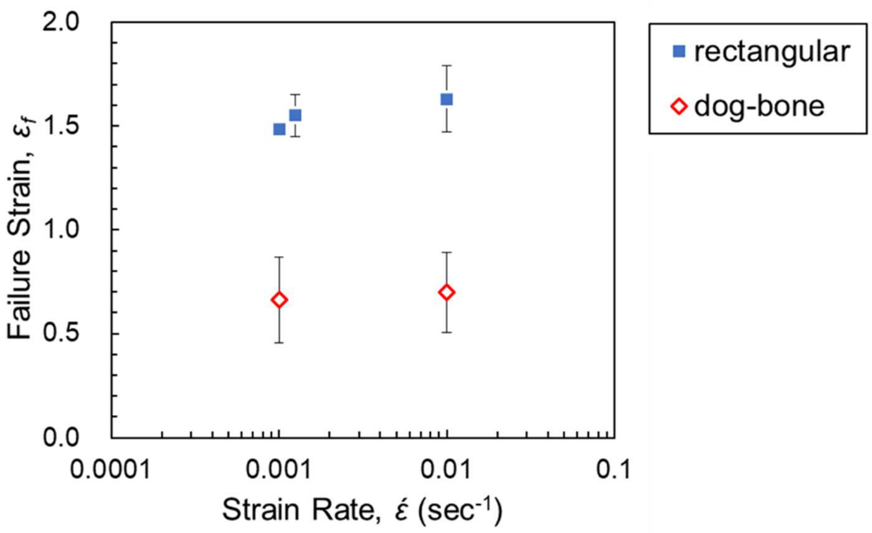

Figure 3.2 Failure strain of dog-bone, and rectangular shaped PET with respect to the strain rate.

Figure 3.3 shows optical microscope images of the dog-bone and rectangular sample. As seen in the images, the edge of the dog-bone shape sample was rougher than that of rectangular. The rough edge of the dog-bone sample presumably causes the stress concentration, leading the decrease in the failure strain.

In this research, substrate with a higher failure strain is favorable because aluminum films cannot be elongated after the fracture of the substrate. Based on the result above, the rectangular shape and the strain rate of 1.25×10^{-3} sec^{-1} were selected as standard testing conditions for this study.

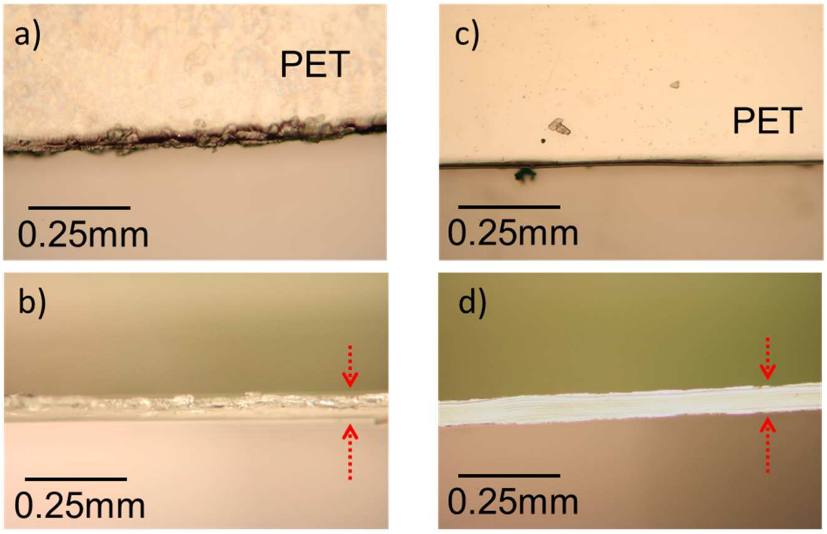

Figure 3.3 Optical microscope images of 25μm-thick PET samples. a) top view and b) cross-sectional view of the dog-bone shape sample. c) top view and d) cross-sectional view of the rectangular shape sample.

The relationship between the actual strain and the apparent strain

DIC images of the 12, 25, and 50 μm-thick PET sample during the tensile test are shown in Figure 3.4. DIC images of 12, and 25 μm-thick PET were successfully obtained up to the deformation of 20 mm. However, the images of 50 μm-thick PET were limited to 7.5 mm because the base painting started to delaminate from the surface of the sample when the applied deformation reached at approximately 7.5mm.

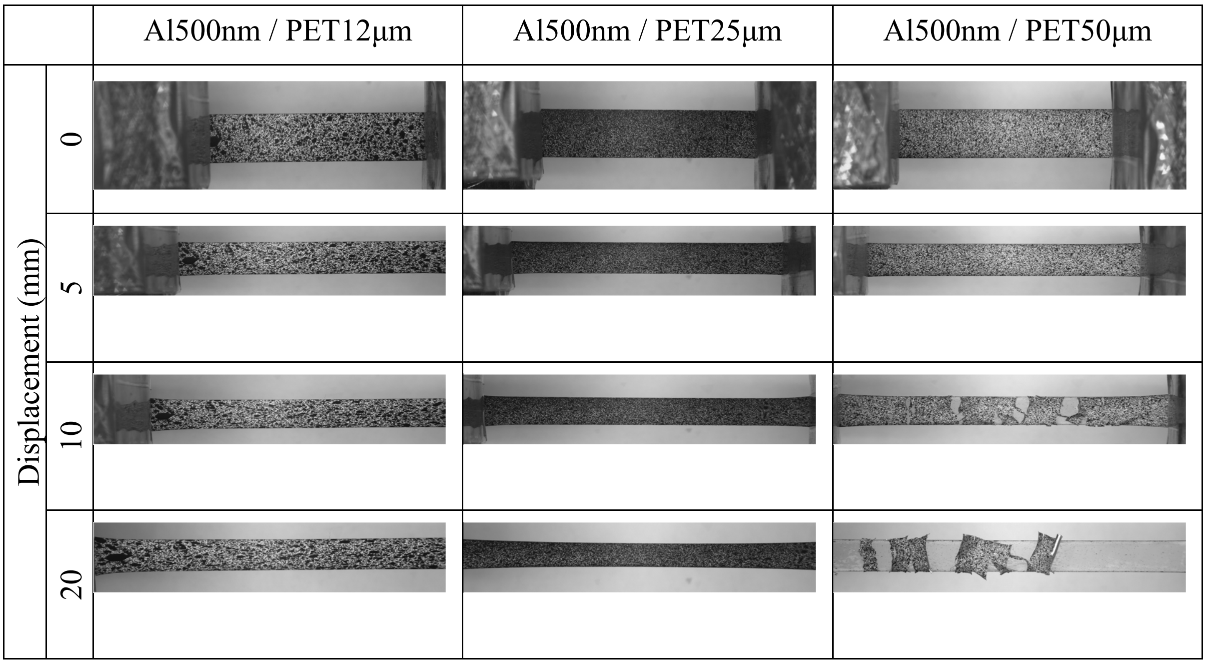

Figure 3.4 DIC images of tensile specimen for DIC analysis.

Figure 3.5 plots the relationship between the strain calculated from the displacement shown in the tensile system (apparent strain, ε_a) and the actual strain calculated using the DIC images (strain, ε). The apparent strain was 93 to 95% of the strain. The 3rd order polynomial curves shown in equation 3.1 to 3.3 were the best fit to the obtained ε_a - ε relationship. The determination coefficient of the fittings was more than 0.999. Hereafter, ε represents the strain converted from ε_a using equation 3.1, 3.2, and 3.3.

$$\varepsilon = -0.3071{\varepsilon_a}^3 + 0.2867{\varepsilon_a}^2 + 0.9841\varepsilon_a - 0.0108 \tag{3.1}$$

$$\varepsilon = -0.0228{\varepsilon_a}^3 + 0.0351{\varepsilon_a}^2 + 1.0174\varepsilon_a - 0.0081 \tag{3.2}$$

$$\varepsilon = -0.9036{\varepsilon_a}^3 + 0.959{\varepsilon_a}^2 + 0.7954\varepsilon_a - 0.0016 \tag{3.3}$$

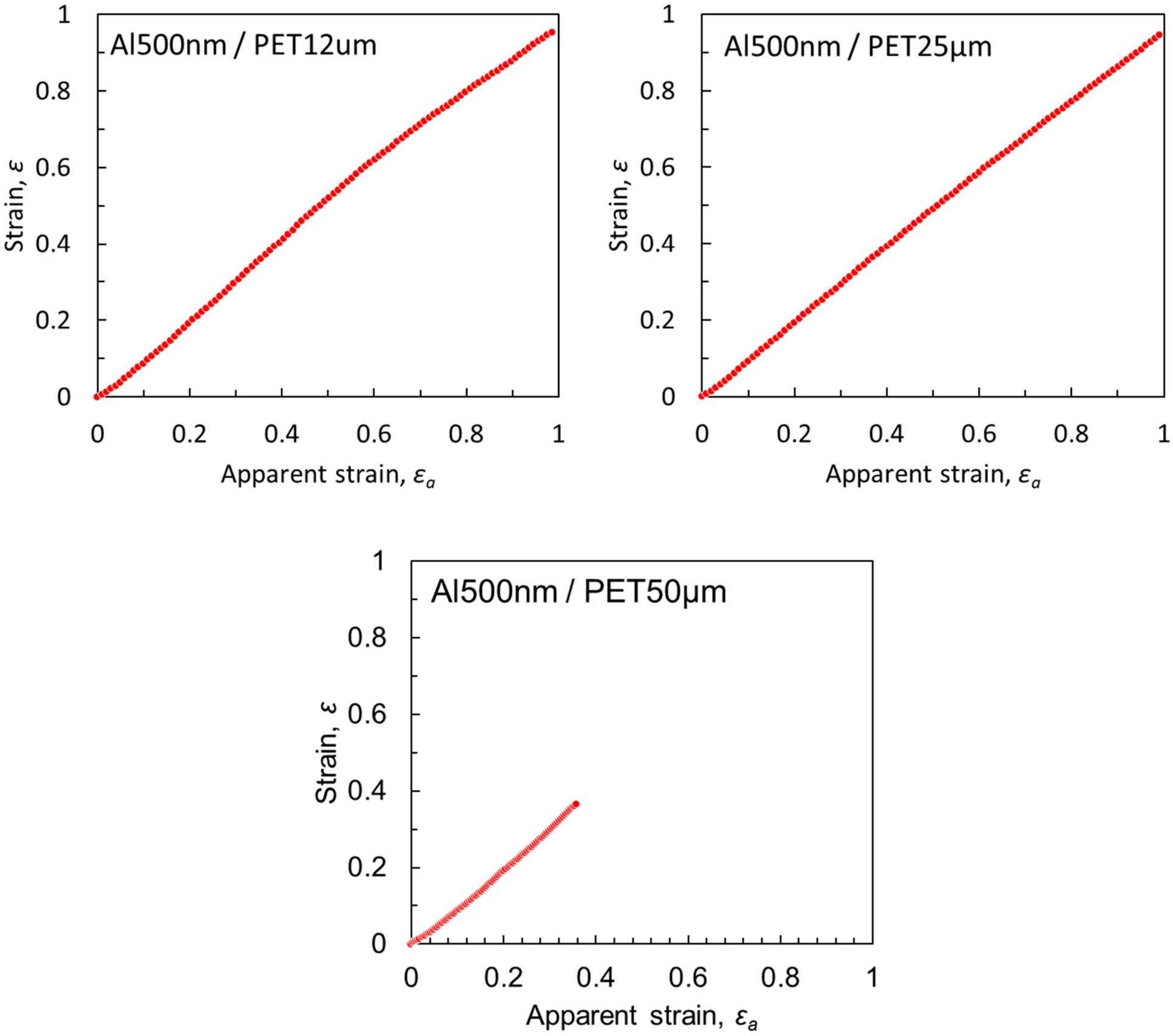

Figure 3.5 The relationship between the apparent strain and the DIC strain for 12, 25, and 50 µm-thick PET with 500 nm thick Al film

Tensile behavior of PET

The typical stress-strain responses of 12, 25, and 50 µm-thick PET are shown in Figure 3.6, and Young's modulus, yield strength, and failure strain of the PET are summarized in Table 3.1 to 3.3.

12 μm-thick PET showed the most steep rise in the stress strain curve in the plastic region, which indicates the high strain hardening. 12 μm-thick PET was highest, and 25 μm-thick PET was lowest in both *E* and σ_Y, and the failure strain of 12μm-thick PET (approximately 1.0) was lower than that of 25, and 50 μm-thick PET (approximately 1.5).

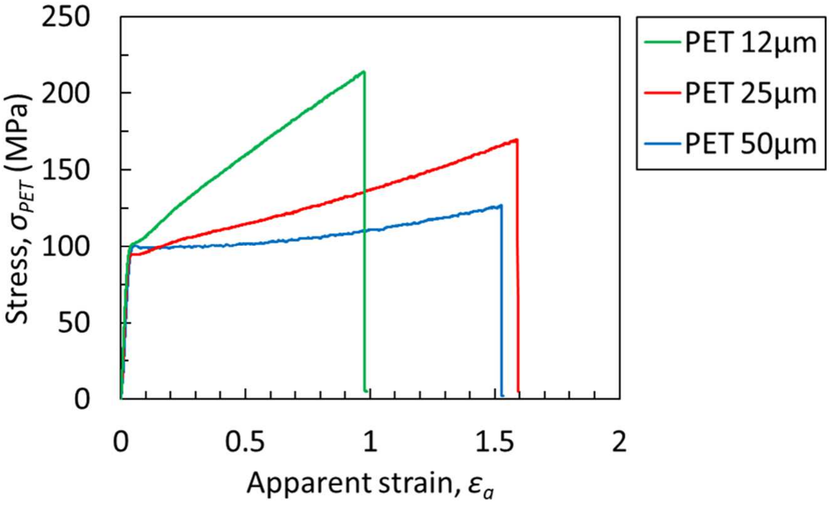

Figure 3.6 Stress strain relationship for 12, 25, and 50 μm-thick PET

Table 3.1 Young’s modulus of PET substrate

	PET 12 μm	PET 25 μm	PET 50 μm
1	3.73	3.30	3.85
2	3.70	3.53	3.91
3	3.96	3.43	3.95
Mean	**3.79**	**3.42**	**3.90**
SD	0.12	0.10	0.04

Table 3.2 Yield strength of PET substrate

	PET 12 μm	PET 25 μm	PET 50 μm
1	98.9	95.8	97.8
2	101.1	95.8	98.8
3	99.9	94.8	99.1
Mean	**100.0**	**95.4**	**98.6**
SD	0.89	0.49	0.54

Table 3.3 Failure strain of PET substrate

	PET 12 µm	PET 25 µm	PET 50 µm
1	0.98	1.47	1.39
2	0.97	1.41	1.53
3	1.09	1.59	1.61
Mean	**1.01**	**1.49**	**1.51**
SD	0.06	0.08	0.09

3. 1. 2 Tensile behavior of Al/PET

Figure 3.7 shows the stress-strain curves, and the change in the electrical resistance of the 500 nm-thick Al film deposited on the 12, 25, and 50 µm-thick PET. Since the thickness of the PET substrate is 25 to 100 times larger than the Al film, the stress-strain response was dominated by PET substrate. Therefore, the sudden drop in stress to 0 indicates the fracture of PET. The electrical resistance before applying the tensile deformation (initial resistance, R_0) of all the samples were ranged from 0.5 to 0.7 Ω. The resistance increased with an increase in the applied strain and jumped up to the infinite when the PET fractured. Al500nm/PET50µm sample showed the highest increase in the resistance regardless of the plasma etching time. Al500nm/PET12µm sample showed the lowest increase when the plasma etching was 3 min, and without plasma etching, Al500nm/PET25μm sample showed the lowest increase when the plasma etching was 5 or 10 min.

As stated in Chapter 2, the theoretical value of the resistance represents the resistance increase due to the decrease in the cross-section caused by the tensile deformation. Thus, the deviation of the experimental resistance from the theory indicates the decrease in the cross-section due to cracks. Assuming the deviation caused by cracks, the failure strain of aluminum film was defined as the point at which the resistance deviates from theoretical value by 5 % [11] [17]. The failure strains are plotted with respect to the plasma etching time in Figure 3.8.

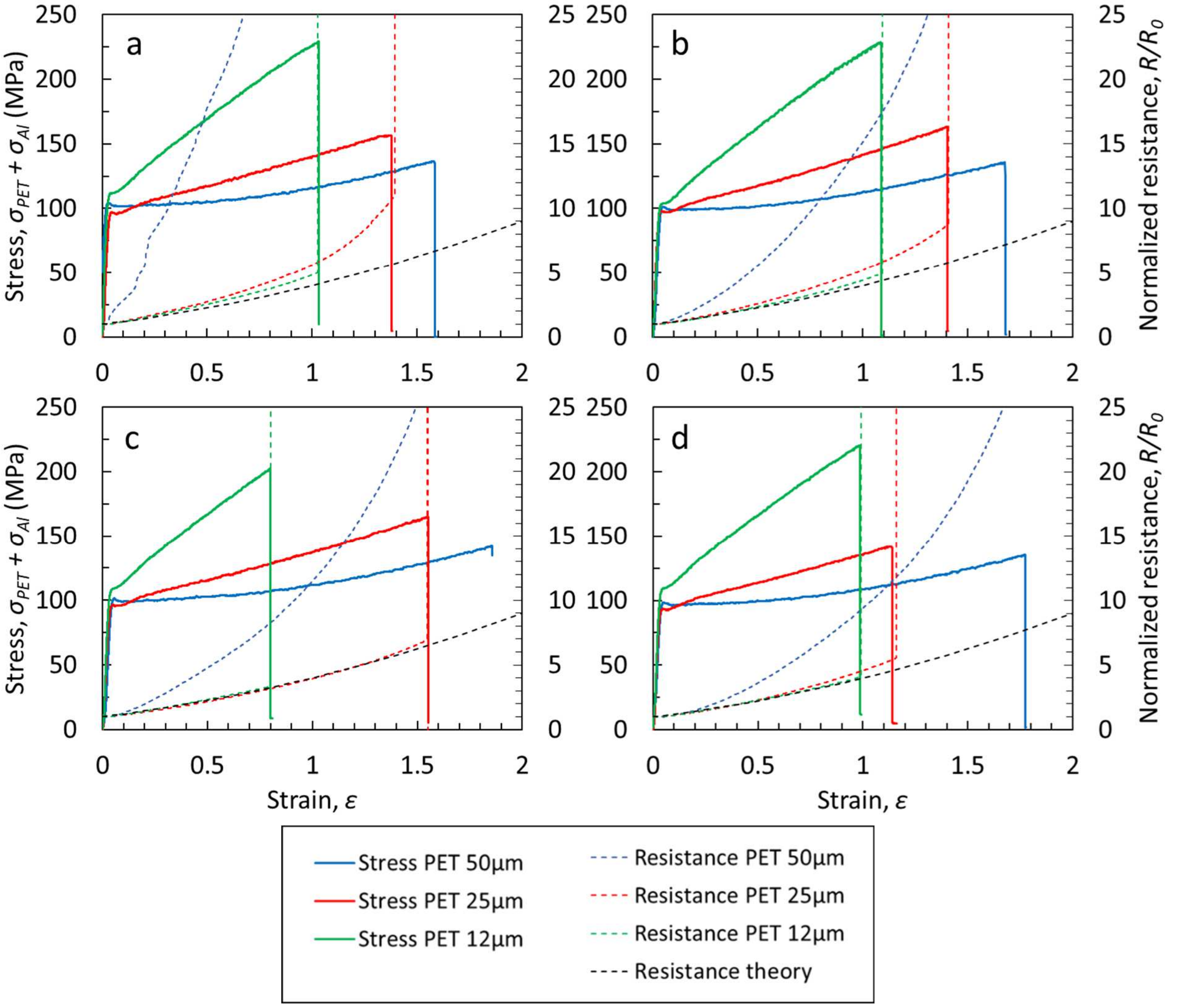

Figure 3.7 Stress-strain curve and the electrical resistance of 500nm-thick Al film deposited on PET substrate a) without plasma etching, b) with 3 min- plasma etching, c) with 5 min-plasma etching, d) 10 min-plasma etching

The failure strain of Al film increased with plasma etching regardless of the thickness of the PET. The failure strain of the Al500nm/PET50μm sample slightly increased as the plasma etching time increased. The failure strain of Al500nm/PET12μm increased with increasing plasma etching time up to 5 min, and slightly decreased when the plasma etching time was 10 min. Al500nm/PET25μm showed maximum when the plasma etching time was 5 min, and the mean value was more than 1.0.

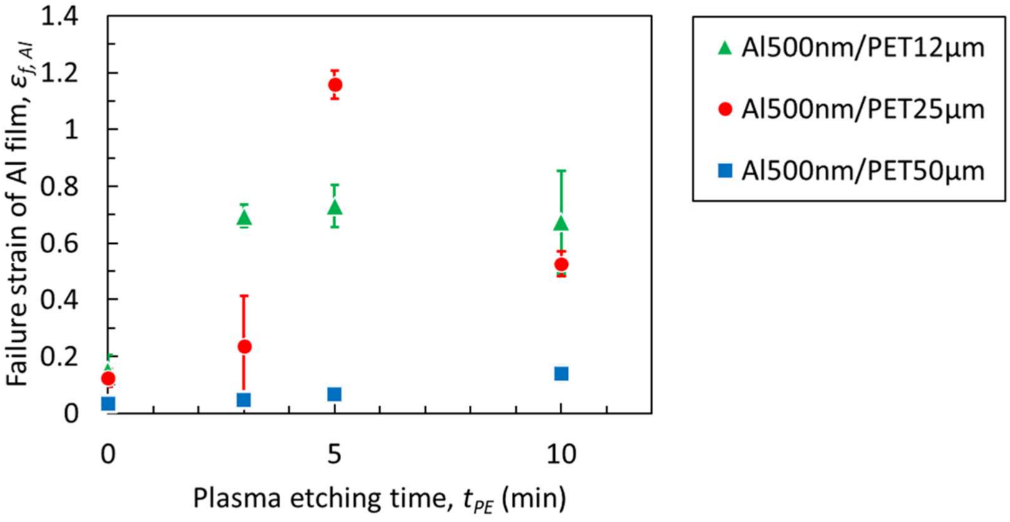

Figure 3.8 Failure strain of Al thin films deposited on PET substrate with respect to the plasma etching time prior to the deposition.

3. 1. 3 Surface observation of Al films after tensile testing sample

The microscopic images of the Al/PET samples with a 0, 5, and 10 min-plasma etching before and after applying a strain are shown in Figure 3.9. Al/PET samples were once loaded to a strain of 0.1, 0.4, 0.8, and 1.0, and then the surface of the Al films was observed after unloading. And the SEM images when the applied strain was 0.8 are also shown in Figure 3.9. The loading direction was along the horizontal direction for all the images.

Tiny dark dots were observed in the Al surface before stretching regardless of the plasma etching time. When the applied strain was 0.1, several dark spots (indicated in the red arrow marks), which were larger than the dark dots, were observed. The tiny dots appeared to start linking each other in the t_{PE} = 0 min-sample. Although the spots were found in t_{PE} = 5, and 10 min-sample as well, the number of the spots was smaller than t_{PE} = 0 min-sample, and linking was not observed. When the applied strain increased to 0.4, cracks were observed in the t_{PE} = 0, and 10 min-sample. The crack aligned to 45° to the loading direction and observed to bridge the dark spot to the other spot. In contrast, no cracks were observed in t_{PE} = 5 min-sample, while the number of spots seemed to increase. When the strain was 0.8, increasing number of the dark spots and cracks were observed in the t_{PE} = 0, and 10 min-sample. From the SEM image, the dark spots were found to be buckles. The cracks linked the buckles in the t_{PE}=0 min-sample and PET was exposed at the cracks. The smaller number of buckles and cracks with exposed PET were also observed in the t_{PE} = 10 min-sample. In contrast, no cracks were observed in t_{PE} = 5 min-sample, and the number of buckles appeared to further decrease. When the strain was 1.0, cracks were further spread in the t_{PE} =10 min-sample. Cracks were also found in t_{PE} = 5 min-sample. However, the cracks were not linked together, and weaker than those in the t_{PE} = 0, and 10 min-sample with a strain of 0.4.

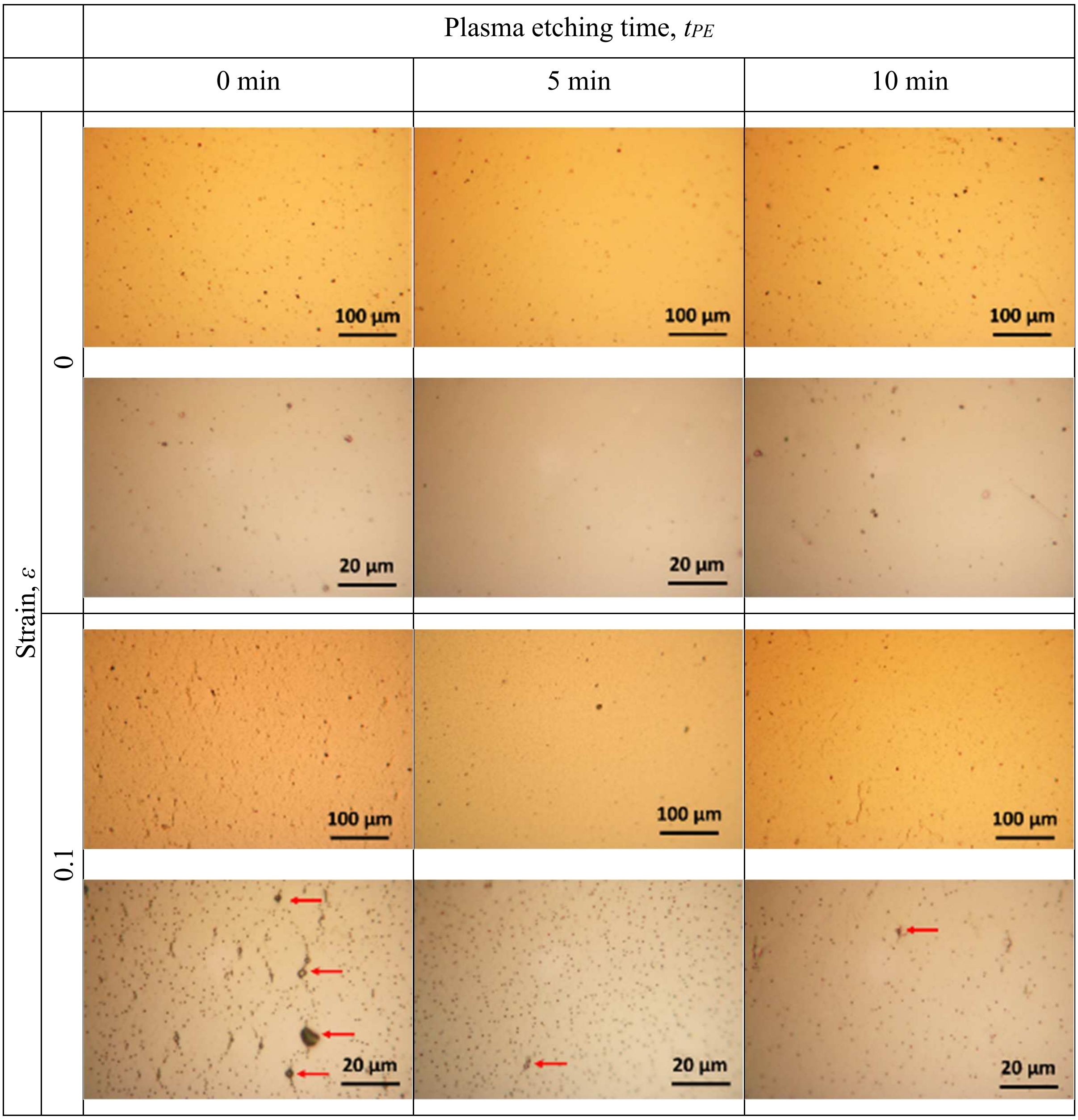
Plasma etching time, t_{PE}
0 min
5 min
10 min
Strain, ε
0
0.1
100 µm
20 µm

	0.4	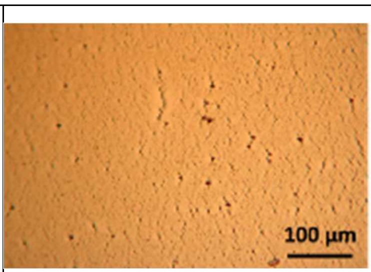	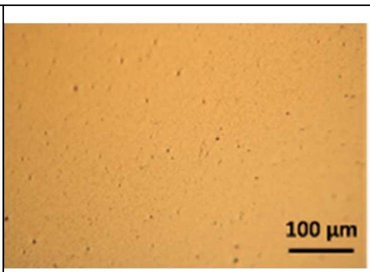	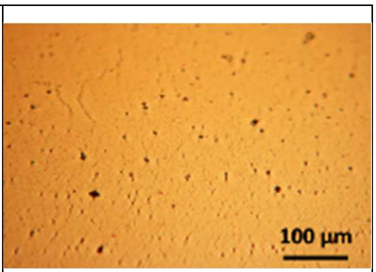
		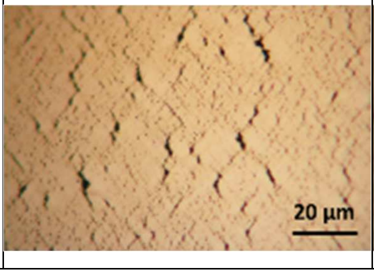	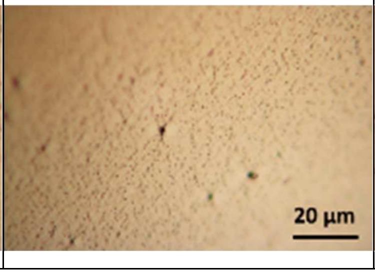	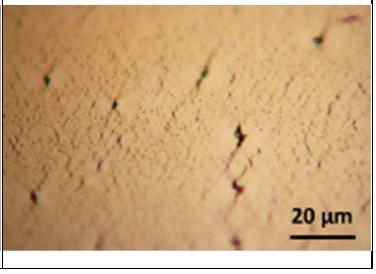

		0.8	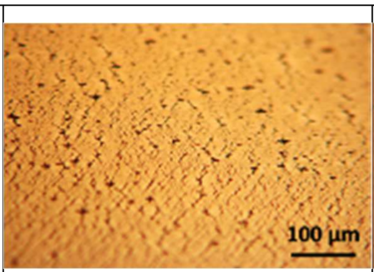100 µm	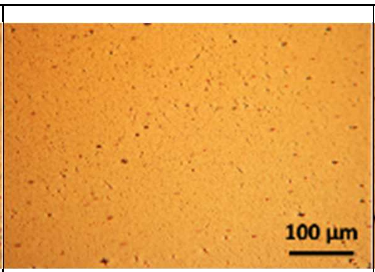100 µm	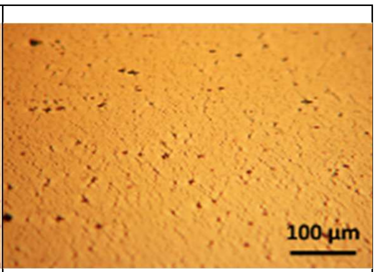100 µm
			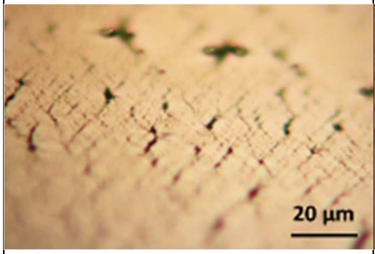20 µm	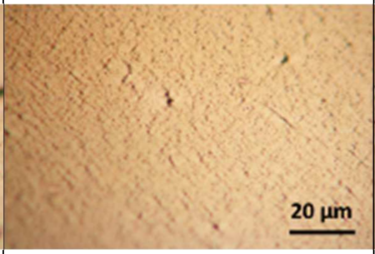20 µm	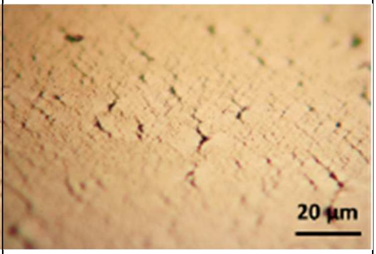20 µm
			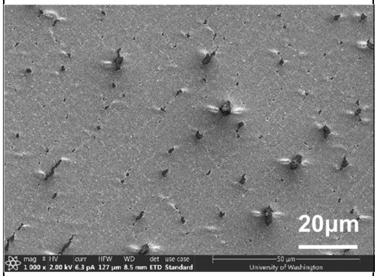20µm	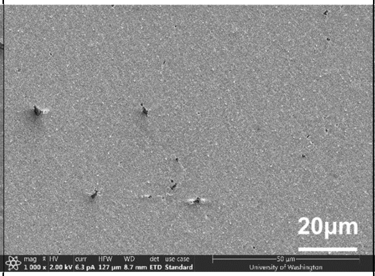20µm	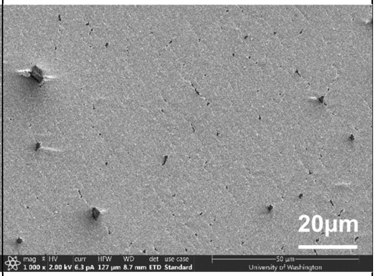20µm
			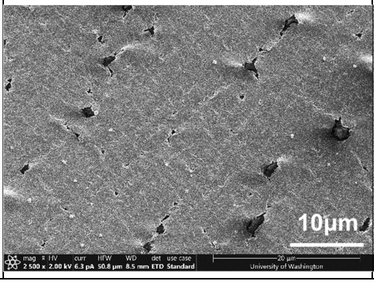10µm	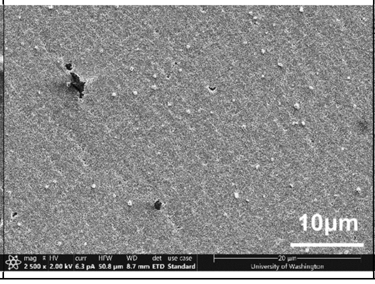10µm	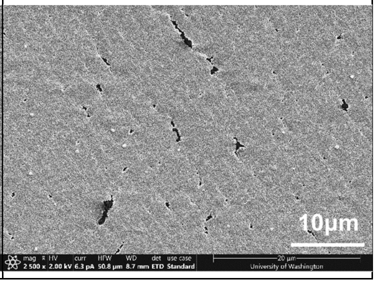10µm

	1.0		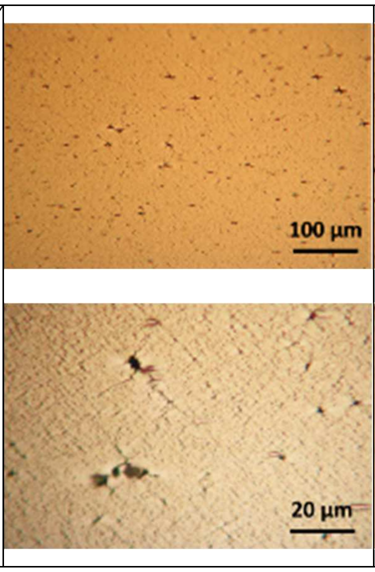	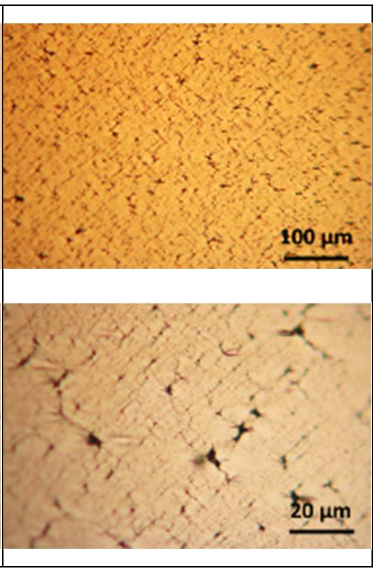

Figure 3.9 The optical microscopy and SEM images of the surface of Al 500nm /PET 25µm sample with a 0, 5, and 10 min-plasma etching after applying a strain. The loading direction is along the horizontal direction.

Figure 3.10 shows the Al surface of 12, 25, and 50 µm-thick PET sample with a 5 min-plasma etching after applying a tensile strain. For the comparison, the same images of 25 µm-thick samples from Figure 3.9 are also shown.

For the 12 µm-thick PET sample, dark spots were found when the applied strain was 0.1, and weak cracks aligned 45 ° to the tensile direction were found with a strain of 0.4. The cracks became clear when the strain increased to 0.8. For the 50 µm-thick PET samples, cracks were observed when the strain was 0.1. With a strain of 0.4, the crack propagated throughout the whole surface, and Al film came off from the PET substrate. Compared under the same applied strain, the fewest spots and cracks were observed in the 25 µm-thick PET samples.

		Al 500nm / PET 12µm	Al 500nm / PET 25µm	Al 500nm / PET 50µm
Strain	0.1	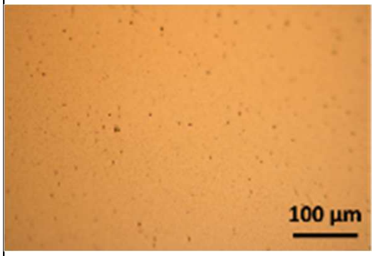	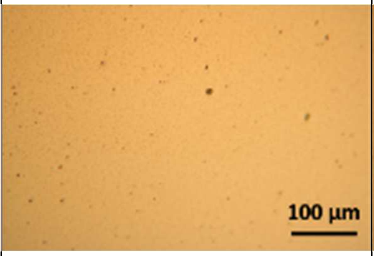	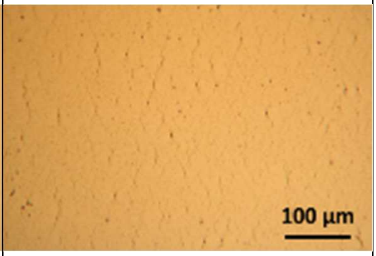
		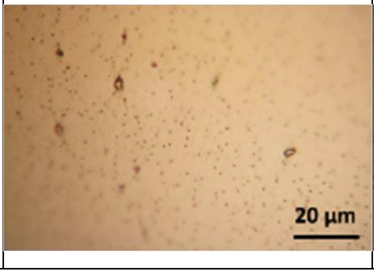	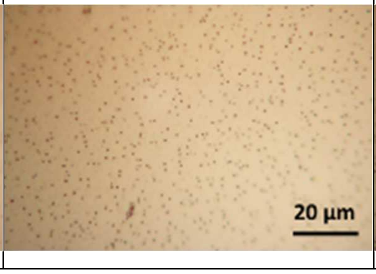	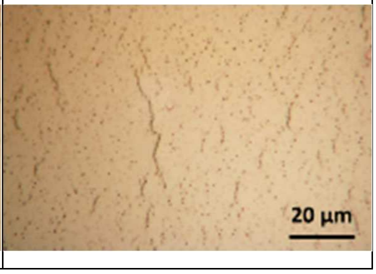

		0.4	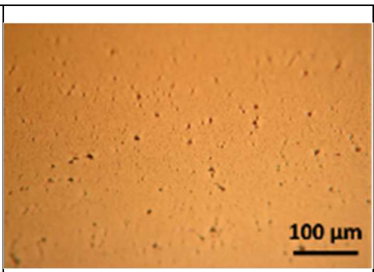 100 µm	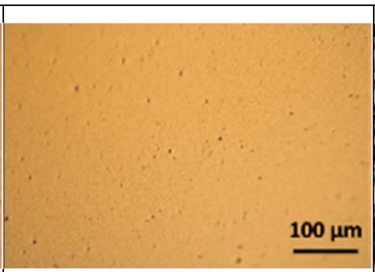 100 µm	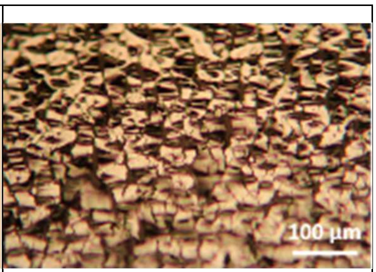 100 µm
			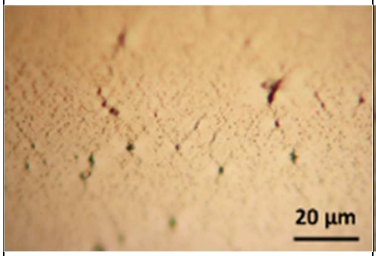 20 µm	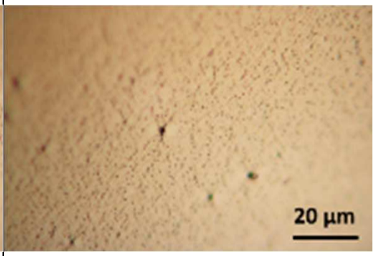 20 µm	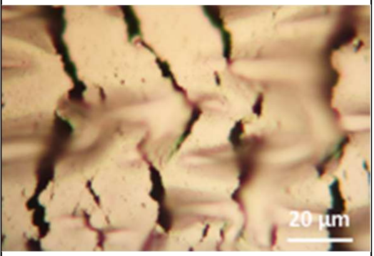 20 µm
			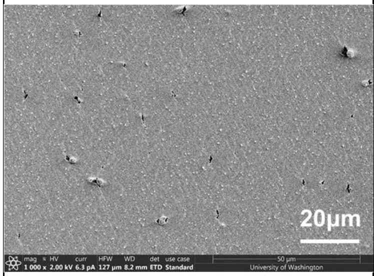 20µm	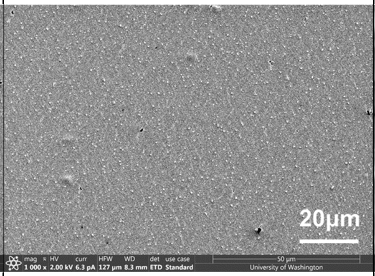 20µm	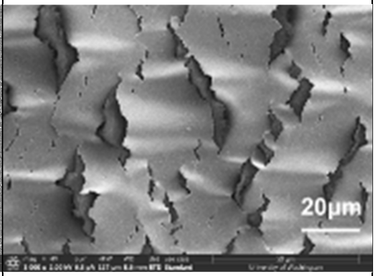 20µm
			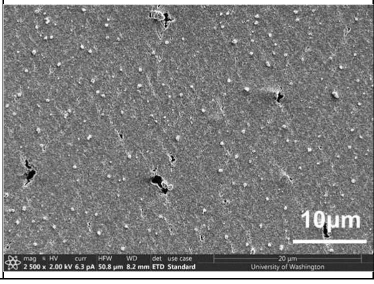 10µm	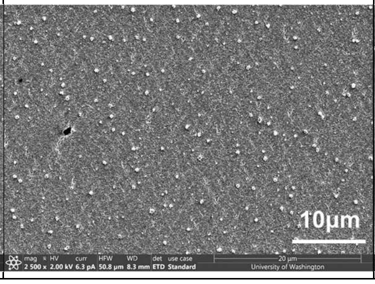 10µm	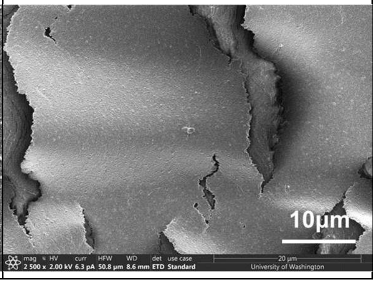 10µm

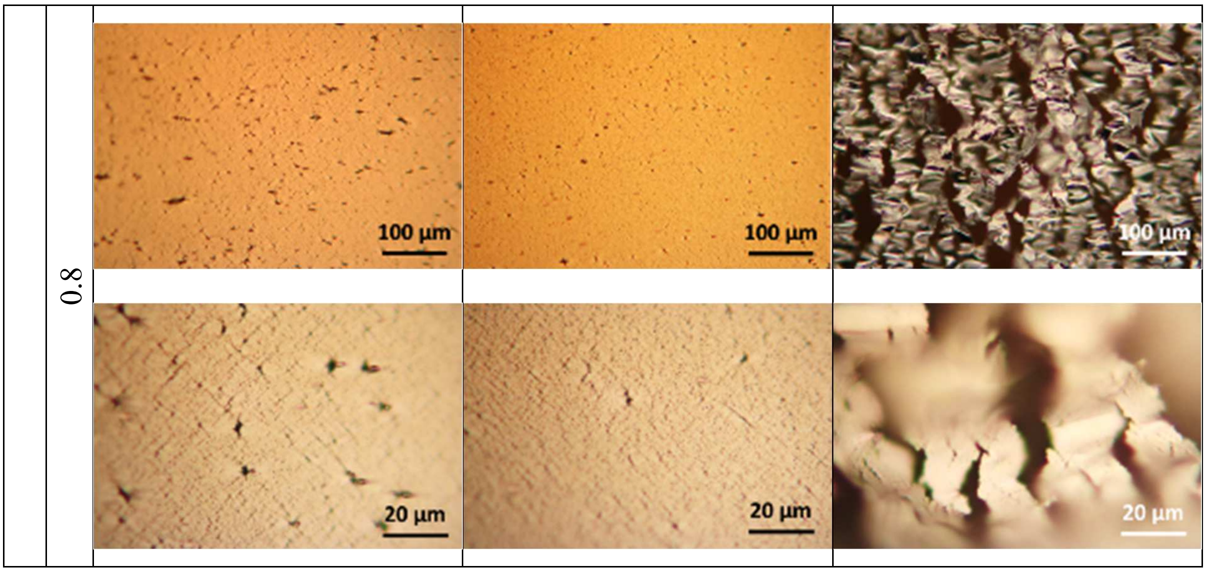

Figure 3.10 The optical microscope and SEM images of the surface of Al 500nm /PET 25µm sample after applying a strain. The loading direction is along the horizontal direction.

3. 2 Interfacial properties of the aluminum film and PET substrate

3. 2. 1 Interfacial strength

Laser spallation of the basic layer structure

The laser spallation test was carried out using the basic layer structure with a 600 nm-thick Al test film deposited on a 0.45mm-thick PET substrate. The pulse laser with an energy of 25 to 260 mJ was focused to a 2 mm-diameter spot on the Al absorbing layer for the stress wave generation, and Ar ion laser with a power of 20 mW was employed for the interferometer. The SEM image and the height profile of the Al surface after inducing the pulse laser are shown in Figure 3.11. When the laser energy was 260 mJ, spallation was observed on the Al film surface. According to the height profile, the height from the bottom of the spallation spot to the Al film was approximately 70 μm. Considering the thickness of the Al film was only 0.6 μm, a part of the PET substrate was spalled away with Al film. A blister was found in the area where the 200, and 150 mJ-energy was used. The height of the blister was 55, and 8μm, respectively. Since the blister was too large for Al thin film to deform without any breaking, Al film probably deformed with a PET substrate, indicating the spallation interface was not between the Al film and the PET substrate, but inside the PET substrate.

Although further spallation test was conducted with an energy less than 150 mJ, the spallation between Al and PET substrate could not be achieved with the basic layer structure sample.

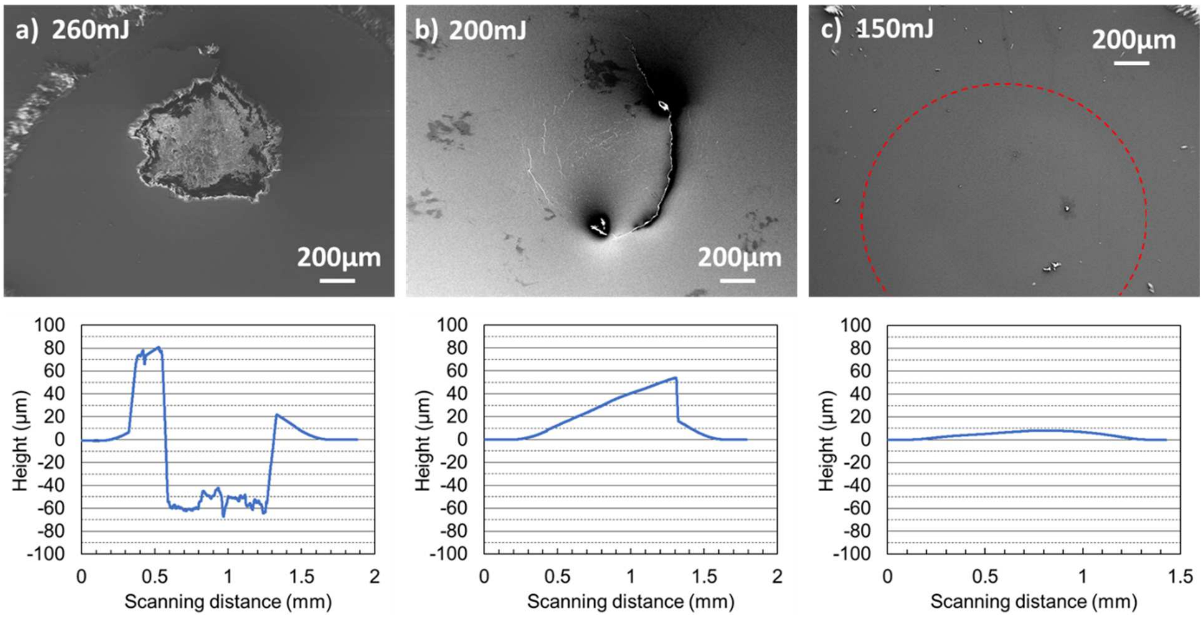

Figure 3.11 SEM images and the corresponding surface profile of the spot of the surface of the Al film after inducing pulse laser with a power of a) 260mJ, b) 200mJ, and c) 150mJ.

Al/PET/SiO_2 structure

The laser spallation test was carried out using the SiO_2 structure with 1500 nm-thick Al test film deposited on a 12, 25, and 50 µm-thick PET substrates. The pulse laser with an energy of 10 to 260 mJ was induced on a 1 mm-diameter spot in the absorbing layer for the spallation, and the power of probing Ar ion laser was 20 mW.

The microscopic images of the spallation spot of Al 2.0μm / PET 50μm / SiO_2 0.6mm (without plasma etching) with the 10 and 260mJ-laser pulse are shown in Figure 3.12. PET exposed under the Al film in the spot with 260 mJ-laser indicates that not only Al film but also PET substrate was spalled away from SiO_2. On the other hand, spalled PET was not observed in the spot with 10 mJ-laser. Therefore, the spallation is considered to occur between Al and PET when the laser energy was 10mJ.

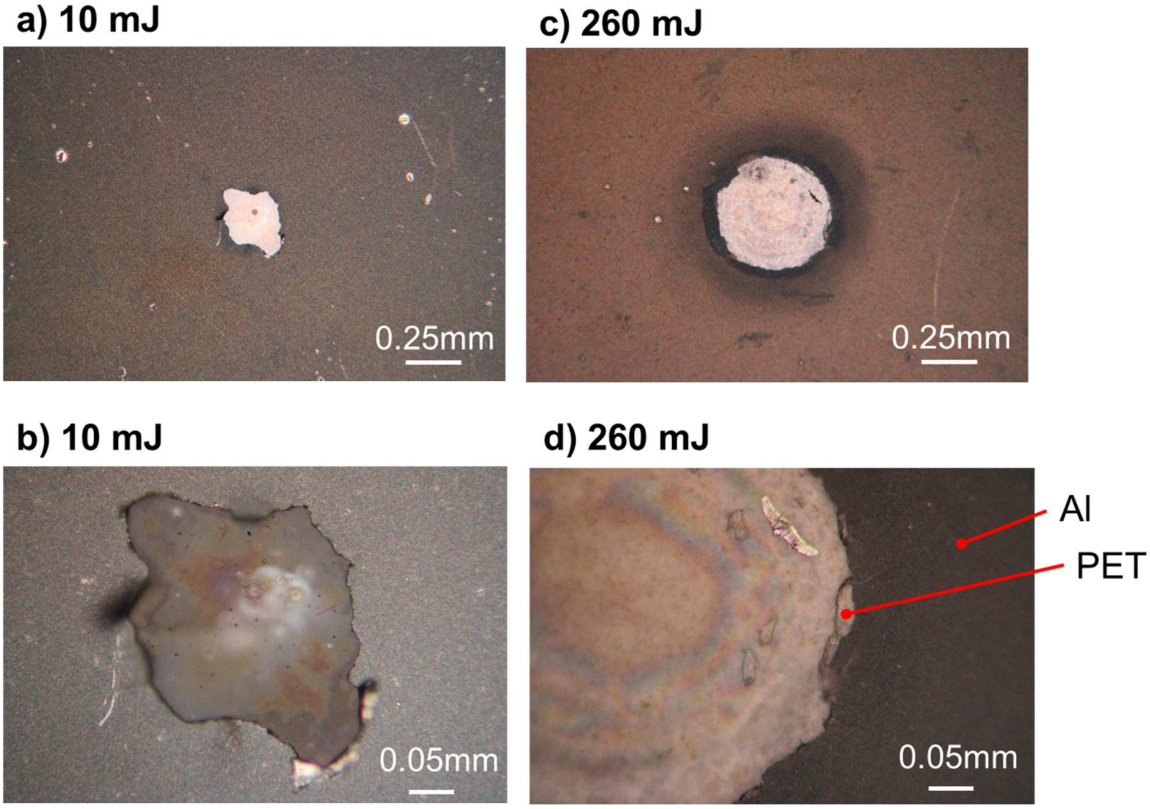

Figure 3.12 Spallation spot for the Al: 2.0μm / PET: 50μm / SiO_2: 0.6mm sample when the laser energy was a), b) 10mJ and c), d) 260mJ. b) and d) are high magnification images of a) and c), respectively.

Based on the result above, additional spallation tests were carried out focusing on the laser energy of around 10 mJ. Figure 3.13 shows the optical microscopic images of the spallation spots for Al: 1.5µm / PET: 50µm / SiO_2: 1.6mm sample with and without plasma etching.

For the sample without plasma etching, Al film was spalled away from the PET with a 10 mJ-laser shot, which was the minimum controllable energy. The area where Al film fully came off became wider with increasing pulsing laser energy. On the other hand, for the sample with 10 min-plasma etching, no spallation spot was observed when the laser energy was 10 to 11 mJ. Unlike the sample without plasma etching, no clear spallation was observed. However, the 15 mJ-shot spalled the tiny area of Al film, and the 20mJ-shot made several tiny spallation areas. When the laser energy was 12.5 mJ, a wrinkle-like trace was observed.

		Without plasma etching	With 10 min-plasma etching
Pulse laser energy (mJ)	10	No spallation observed	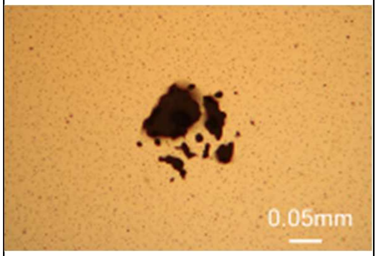
	11	No spallation observed	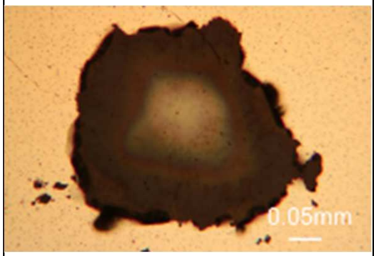
	12.5	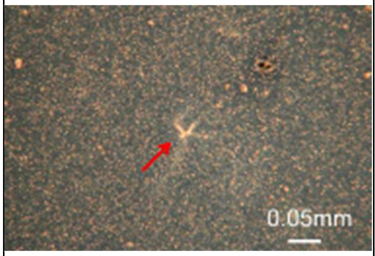	Not Tested
	15	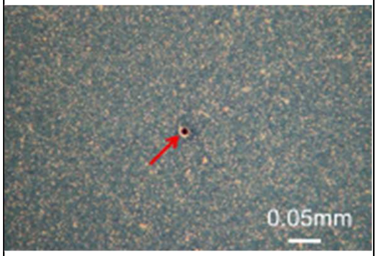	Not tested
	20	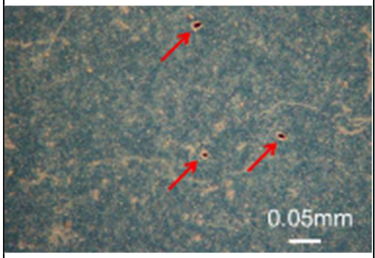	Not tested

Figure 3.13 Typical spallation images for Al: 1.5µm / PET: 50µm / SiO_2: 1.6mm sample with and without plasma etching

The fringe data corresponding to the spallation spots in the Figure 3.13 are shown in Figure 3.14. No fringe data was obtained when the energy was 10mJ. Clear fringes were obtained with the energy of 11 to 20 mJ, the number of fringes within 100 ns increased as the energy increased indicating an increasing stress magnitude.

<table>
<tr><td></td><td></td><td>Without plasma etching</td><td>With 10 min-plasma etching</td></tr>
<tr><td rowspan="2"></td><td>11</td><td>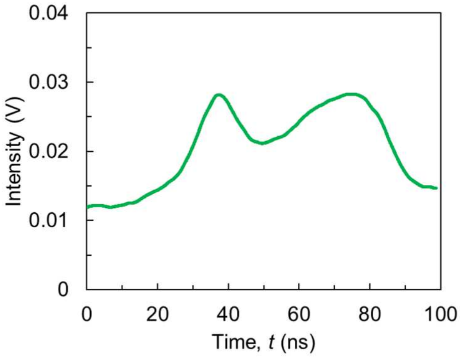
</td><td>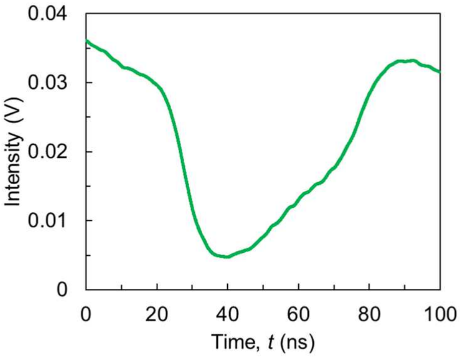
</td></tr>
<tr><td>12.5</td><td>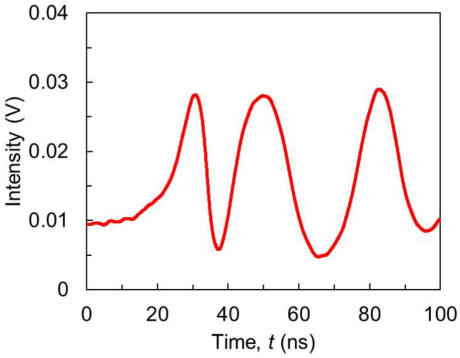
</td><td>Not tested</td></tr>
</table>

	15	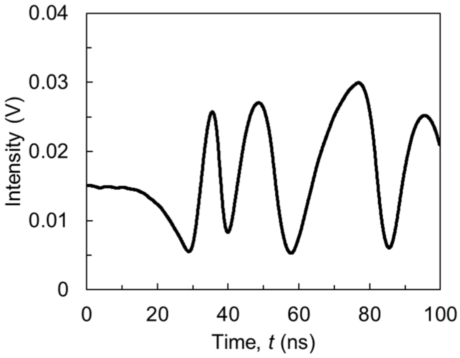	Not tested
	20	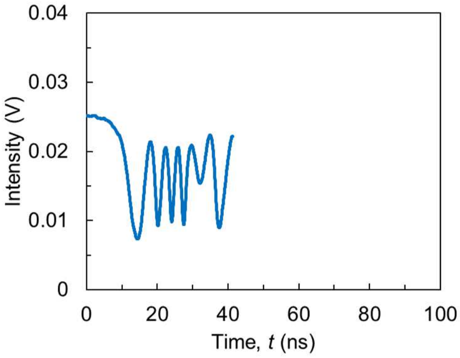	Not tested

Figure 3.14 The fringe data for 50µm-thick PET sample with/without plasma etching.

Figure 3.16 shows the displacement, and stress profiles obtained by processing the fringe data in Figure 3.14. The maximum compressive stress in Figure 3.15 (b) reached the maximum approximately 27 ns after the wave arrival at 0 ns, and showed the steep rising. These characteristics of the stress profile were formed due to the non-linear elastic properties of SiO_2 as stated in the studies using fused silica [37] [25]. The steep rising part made the maximum tensile stress in Figure 3.15 (c).

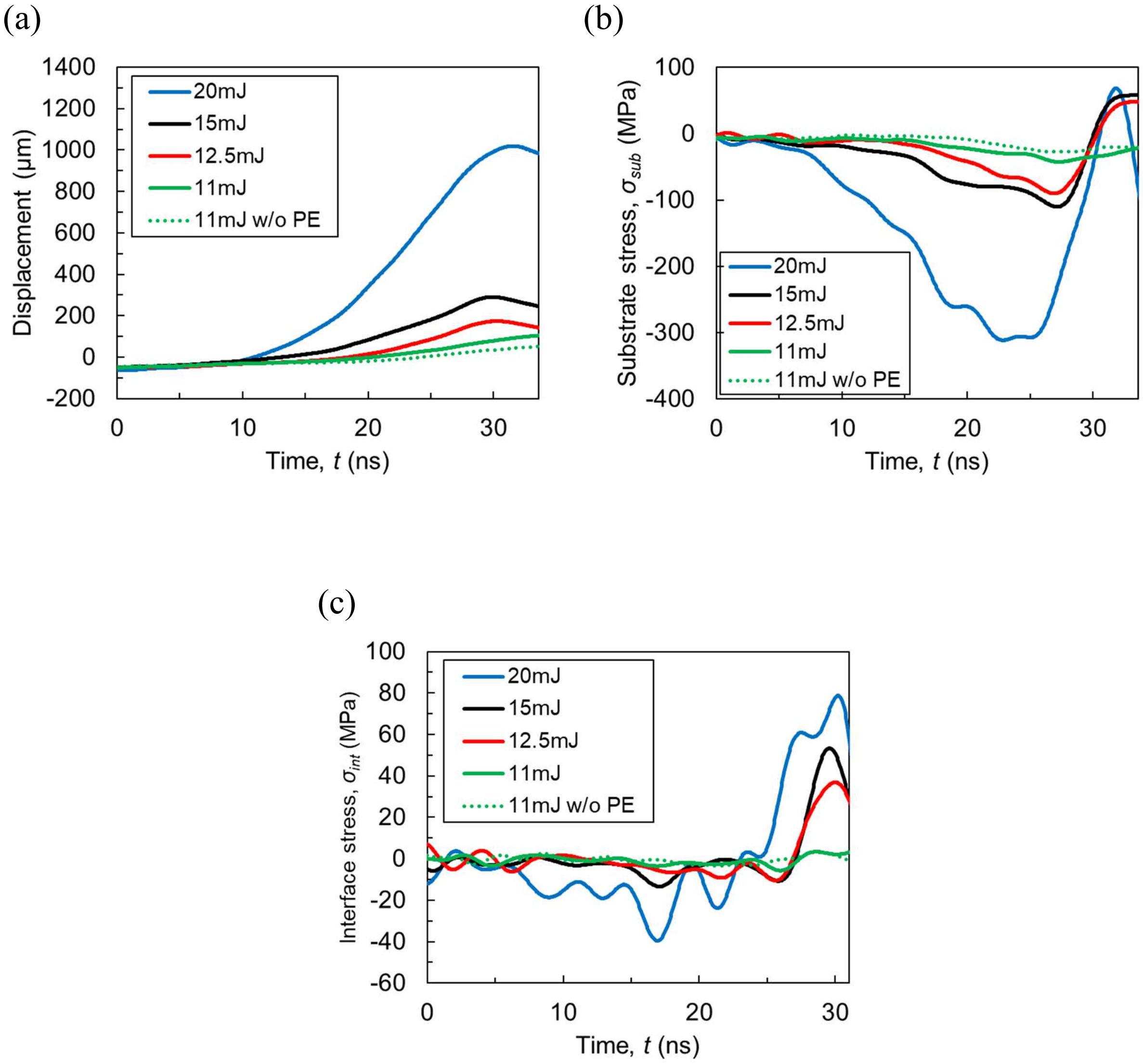

Figure 3.15 Data profile for 50μm-thick PET sample with/without plasma etching (a) displacement profile (b) substrate stress profile (c) interface stress profile

Figure 3.16 shows the interface stresses of the 50 μm-thick PET sample with and without plasma etching as a function of the laser energy. The interfacial adhesion can be determined as the maximum σ_{int} without spallation. Based on the result above, σ_{int} for the sample without plasma etching was considered as was less than 5.3 MPa and cannot be specified because even the minimum energy shot made a clear spallation. For the sample with 10 min-plasma etching, 12.5 mJ was the maximum laser energy without spallation. Therefore, the interfacial adhesion of the sample was determined as 37 MPa from Fig. 3.15c.

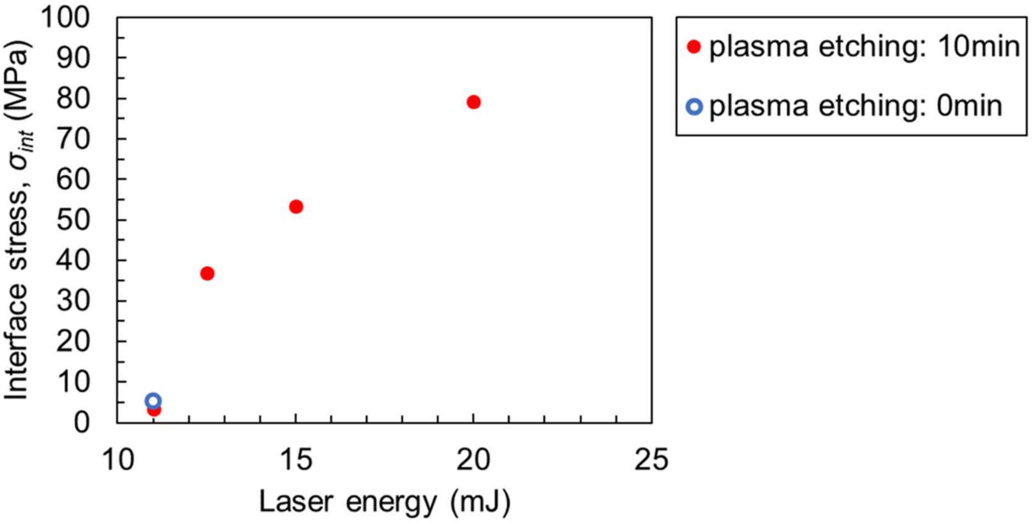

Figure 3.16 Interfacial stress for 50μm-thick PET sample with/without plasma etching with respect to the laser energy.

3. 2. 2 Surface morphology of PET

Figure 3.17 shows the surface roughness of 12, 25, 50 µm-thick PET substrates obtained from the AFM analysis with respect to the plasma etching time. It was expected that the surface profile was unique to each other for 12, 25, and 50 µm-thick PET because a different thickness of PET was possibly manufactured through a different process. However, there was no significant difference in the value of the surface roughness among the three different thicknesses of PET. In addition, the roughness value did not substantially change after applying the plasma etching and was ranged within 2 to 10 nm regardless of the plasma etching time.

AFM micrographs of the surface of 25 µm-thick PET with a plasma etching are shown in Figure 3.18. Although there was no difference in the roughness value, micrographs showed a change as the plasma etching time increased. That is, periodic swell with a frequency of 1 µm along the x-direction was observed when the plasma etching time was 30min. The weak similar swell was also observed in the PET with 10 min-plasma etching. The swell was observed more clearly in the surface line profile of the AFM images shown in Figure 3.19. When the plasma etching time was 0, and 5 min, the swell appeared to be faint.

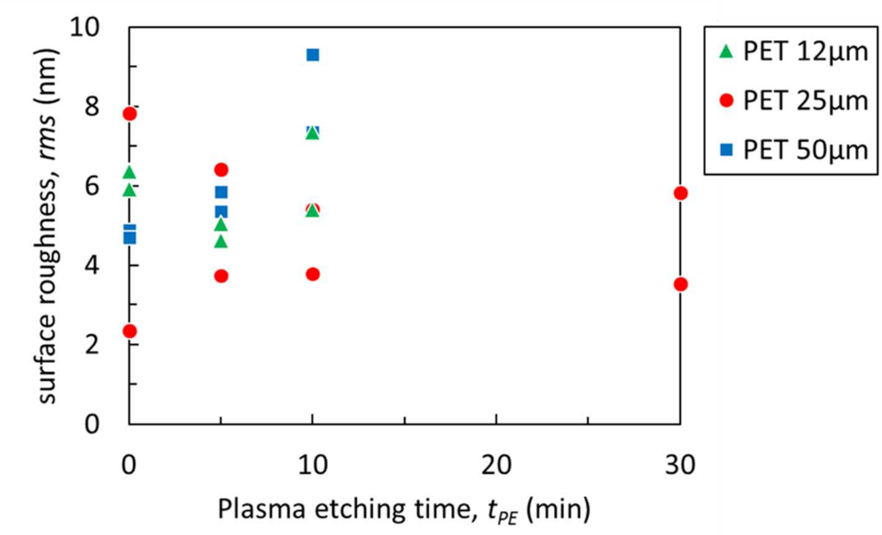

Figure 3.17 Surface roughness of the PET as a function of plasma etching time

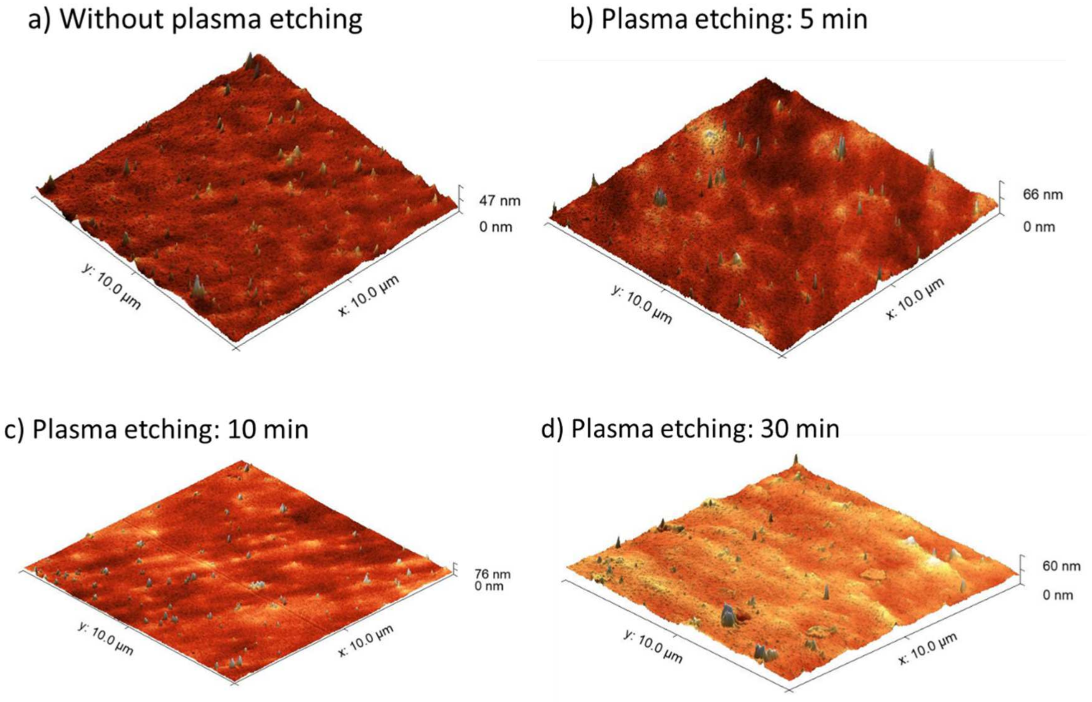

Figure 3.18 AFM images of 25µm-thick PET substrate a) without plasma etching b) with 5 min-plasma etching c) 10 min-plasma etching d) 30 min-plasma etching

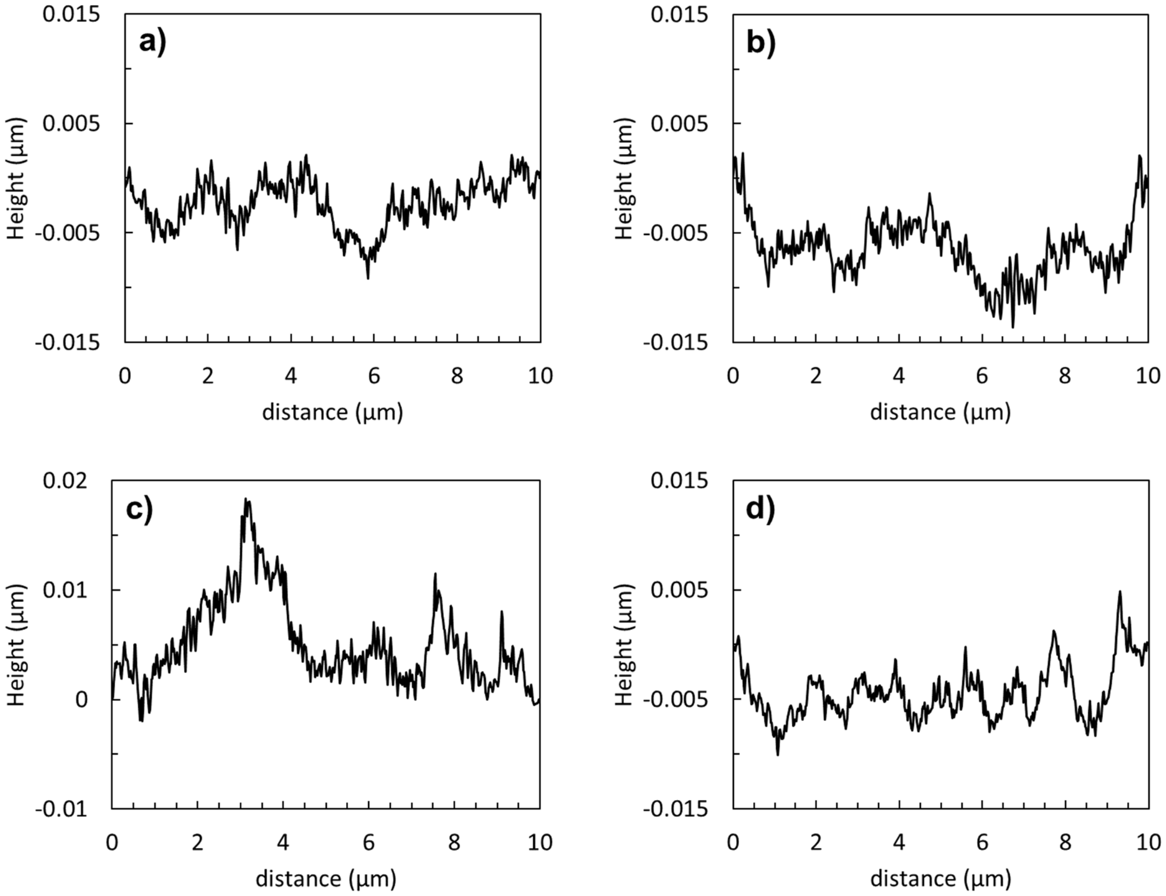

Figure 3.19 Surface line profile of 25μm-thick PET substrate. a) without plasma etching b) with 5 min-plasma etching c) with 10 min-plasma etching d) with 30 min plasma etching

3. 2. 3 Contact angle of water on PET

Figure 3.20 shows the contact angle of water on the PET substrate as a function of the plasma etching time. The contact angle decreased from 70-80 degree without plasma etching to approximately 40 degree at a 5 min-plasma etching. There is no significant difference between the angle with 5, and 10 min plasma etching. The angles of 12, 25, and 50 µm-thick PET were similar to each other at the same plasma etching time.

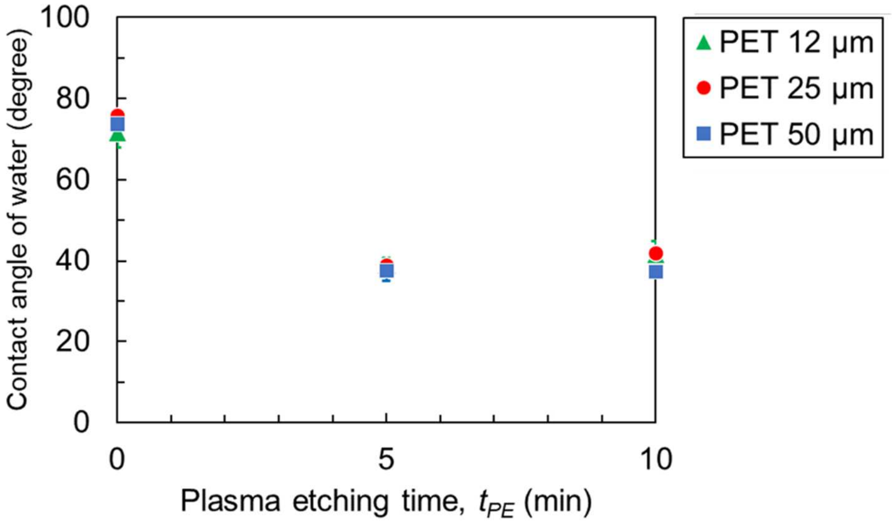

Figure 3.20 The contact angle of water on the PET substrate as a function of plasma etching time.

Chapter 4. Discussion

4. 1 Effect of the plasma etching on the interfacial adhesion

The laser spallation technique was applied to quantitatively evaluate the interfacial adhesion of Al and PET. Although the interfacial adhesion of Al and PET without plasma etching cannot be specified, it was confirmed that the adhesion substantially increased from less than 5.3 MPa to 37 MPa after applying the 10 min-plasma etching.

The mechanism of the chemical state modification and improvement of the adhesion may be assumed as follows. During the plasma etching process, Ar ion attacked the repeating unit of PET, including the C-O and C=O bonding, leaving behind radicals such as O·, and C-O·[29]. The decrease in the contact angle water indicates the existence of the radicals in the surface of the PET after plasma etching. Then these radicals form Al-O-C bonding with Al at the beginning of the sputtering deposition. As stated in the Bou's study [38], the formation of the Al-O-C bonding increases the adhesion between Al and PET.

In addition, AFM analysis in this research indicates the plasma etching modifies the PET surface not only in chemically, but also physically. While the area average roughness did not different before and after plasma etching, the periodic swell was observed in the line scanning profile when the plasma etching time was 10, and 30 min. The periodic swell may contribute to the improvement in the interfacial adhesion by mechanical interlocking.

4. 2 Tensile behavior of Al film

For Al 500nm / PET25μm with 5 min-plasma etching, the deviation of the resistance from the theory was less than 2% even when the applied strain was 1.0. In other words, the Al / PET did not fail based on the definition of this research. However, buckles were found in the microscopic image at the strain. During the tensile test, PET substrate shrinks more in width than Al film due to its' high Poisson's ratio (Al: 0.31, PET: 0.43 [18]). Accordingly, Al film may not be able to follow the shrinkage of PET when the tensile deformation was large, and delaminated from PET. It is thought that the buckles were formed due to the delamination. At the buckles, Al appeared to have ruptured and is no longer conductive. However, the crack propagations from the buckles were short, and the cracks did not bridge the buckle to another. As a result, the decrease in the cross-section was limited, and the resistance did not increase significantly.

On the other hand, for the same structure sample without plasma etching, cracks spread over the surface when the strain was larger than 0.4. In addition, each crack appeared to be deeper than the one found in the PET sample. From the observation, it is thought that these cracks decreased the cross-section in depth and width, leading to a substantial increase in the resistance, and a large deviation from the theoretical resistance.

4. 3 Effect of interfacial adhesion on ductility of Al film

The failure strain of Al film increased by applying the plasma etching regardless of the thickness of the PET. Considering the result of the laser spallation test and the contact angle measurement, the increase in the interfacial adhesion contributed to the increase in the failure strain.

When Al/PET is subjected to the tensile deformation, strain of Al and PET are equal to each other as long as the applied tensile load is distributed uniformly through the entire thickness of the Al/PET laminate. However, once the strain localization is initiated due to the defects or imperfections in the Al films, traction will arise at the interface of Al and PET [6]. According to the shear lag theory, the load acting on the PET substrate will be transferred to Al film through shear stress at the interface in the area [39] [40]. It is assumed that the shear stress causes local delamination of Al film from PET substrate when the interfacial adhesion is weak, such as the sample without plasma etching. PET was not able to retard the strain concentration in Al film after the delamination. As a consequence, Al film easily ruptured, similar to the free-standing metal film.

The failure strain of 25μm-thick PET with 10 min-plasma etching was lower than the one with 5 min plasma etching. There may be two possible scenarios causing the degradation of the failure strain of Al film. One is that the etching could damage the surface of the PET by heating, as indicated in Pelagade's study [30], causing a decrease in the interfacial adhesion. However, the result of the contact angle measurement indicates that 10 min plasma etching did not bring severe damage to the surface of the PET. The other one is that the etching could increase the surface roughness of the substrate, leading to a strain concentration in the metal film. The line surface profile revealed that the plasma etching made a periodic swell, and the swell became clear as the etching time increased. It is possible that the swell could be a cause of the stress concentration, leading to a decrease in the failure strain of the Al film.

In summary, plasma etching improved the interfacial adhesion of Al and PET due to the modification of the chemical state of the PET surface. The effect reached saturation when the plasma etching time was 5 min. On the other hand, the plasma etching formed periodic swell on the surface of the PET. The swell appeared to be more prominent as the plasma etching time increases and might decrease the failure strain of Al by initiating stress concentration during the tensile test. Due to the combination of the two effects, the failure strain of the Al film exhibited the maximum value when the plasma etching time was 5 min.

4. 4 Effect of PET thickness on the ductility of Al film

The failure strain of Al film significantly varied with the thickness of PET substrate even though the results of the contact angle measurement indicate that interfacial adhesion were not substantially different from each other.

As stated in the previous section, shear stress at the interface plays an important role on the failure strain of Al film. According to the shear lag assumption, the shear stress is proportional to the load acting on the substrate [39] [41]. Thus, the thicker the substrate, the higher the shear stress. Consequently, it is assumed that the interfacial adhesion is strong enough to prevent a delamination caused by shear stress when PET thickness is 12 and 25. However, when the thickness of PET is 50μm, the shear stress is higher than that in the 12 and 25μm PET sample. Then the adhesion is not strong enough to tolerate the shear stress even for the case of improved adhesion by plasma etching.

Chapter 5. Conclusions and Future Work

5. 1 Conclusions

Al films sputtered on PET substrate with varying interfacial adhesion were produced by controlling the time of the plasma etching prior to the Al deposition. The ductility of the Al films and the interfacial adhesions of the Al film and PET substrate were evaluated to discuss the effect of the adhesion on the ductility of the Al film. In addition, the effect of the thickness of the substrates was investigated using substrates with different thicknesses. Based on the results of the uniaxial tensile test, laser spallation test, and surface analysis, the following conclusions can be drawn.

- Plasma etching improved the ductility of the Al film. As a result of the parametric study, the most effective plasma etching time was found to be 5 min for Al film with 12, and 25 μm -thick PET substrate.

- Failure strain of Al film with 50 μm-thick PET substrate was substantially lower than that with the 12, and 25 μm-thick PET.

- Surface observations with optical microscope and SEM revealed large number of voids and cracks in Al film without plasma etching and Al film with 50 μm-thick PET, indicating low ductility. The results agreed well with the that from the tensile tests.

- Effects of the plasma etching, and substrate thickness can be explained by the shear lag theory. Thus, loading on the PET substrate is transferred to the Al film through shear stress at the interface near crack region. The plasma etching improves the interfacial adhesion strong enough to tolerate the shear stress. Higher load on the thicker substrate causes higher shear stress, leading to the delamination.

- Laser spallation test revealed that the interfacial adhesion of Al film and PET substrate increased from less than 5.3 MPa to 37 MPa by applying the 10 min-plasma etching. The contact angle measurement and AFM analysis on the surface of the PET substrate indicate the chemical and physical changes in the PET surface were responsible for the improvement of the interfacial adhesion.

5. 2 Future work

This research revealed that plasma etching is a promising method to improve the interfacial adhesion of Al film and PET substrate. However, the optimization on the plasma etching conditions may further increase the adhesion. The conditions include the etching power, processing gas pressure, and the gas material. The optimized conditions will be able to enhance the ductility of the Al film, and may be useful for other thin metal films.

The tensile behavior of the single layer of Al film was employed in this research. However, most of the application of the metal film requires the multi-layer structure in practice. Thus, the future research should include the mechanical behavior of multi-layer metal films. The findings in this research could provide some guidance for the future multi-layer research.

Bibliography

[1] P. Heremans, A. K. Tripathi, A. de Jamblinne de Meux, E. C. Smits, B. Hou, G. Pourtois, and G. H. Gelinck, "Mechanical and Electronic Properties of Thin-Film Transistors on Plastic, and Their Integration in Flexible Electronic Applications," *Adv Mater,* vol. 28, no. 22, pp. 4266-82, Jun, 2016.

[2] K. Xie, and B. Wei, "Materials and structures for stretchable energy storage and conversion devices," *Adv Mater,* vol. 26, no. 22, pp. 3592-617, Jun 11, 2014.

[3] D. P. J. Cotton, I. M. Graz, and S. P. Lacour, "A Multifunctional Capacitive Sensor for Stretchable Electronic Skins," *IEEE Sensors Journal,* vol. 9, no. 12, pp. 2008-2009, 2009.

[4] M. A. Phillips, B. M. Clemens, and W. D. Nix, "A model for dislocation behavior during deformation of Al/Al3Sc (fcc/L12) metallic multilayers," *Acta Materialia,* vol. 51, no. 11, pp. 3157-3170, 2003.

[5] H. Espinosa, "Plasticity size effects in free-standing submicron polycrystalline FCC films subjected to pure tension," *Journal of the Mechanics and Physics of Solids,* vol. 52, no. 3, pp. 667-689, 2004.

[6] Y. Xiang, T. Li, Z. Suo, and J. J. Vlassak, "High ductility of a metal film adherent on a polymer substrate," *Applied Physics Letters,* vol. 87, no. 16, pp. 161910-1 - 161910-3, 2005.

[7] M. Ben Bettaieb, and F. Abed-Meraim, "Investigation of localized necking in substrate-supported metal layers: Comparison of bifurcation and imperfection analyses," *International Journal of Plasticity,* vol. 65, pp. 168-190, 2015.

[8] B. Putz, C. May-Miller, V. Matl, B. Völker, D. M. Többens, C. Semprimoschnig, and M. J. Cordill, "Two-stage cracking of metallic bi-layers on polymer substrates under tension," *Scripta Materialia,* vol. 145, pp. 5-8, 2018.

[9] B. Zhang, T. Y. Xiao, X. M. Luo, X. F. Zhu, and G. P. Zhang, "Enhancing fatigue cracking resistance of nanocrystalline Cu films on a flexible substrate," *Materials Science and Engineering: A,* vol. 627, pp. 61-64, 2015.

[10] D. Faurie, P. O. Renault, E. Le Bourhis, G. Geandier, P. Goudeau, and D. Thiaudière, "Mastering the biaxial stress state in nanometric thin films on flexible substrates," *Applied Surface Science,* vol. 306, pp. 70-74, 2014.

[11] N. Lu, Z. Suo, and J. J. Vlassak, "The effect of film thickness on the failure strain of polymer-supported metal films," *Acta Materialia,* vol. 58, no. 5, pp. 1679-1687, 2010.

[12] R. M. Niu, G. Liu, C. Wang, G. Zhang, X. D. Ding, and J. Sun, "Thickness dependent critical strain in submicron Cu films adherent to polymer substrate," *Applied Physics*

Letters, vol. 90, no. 16, pp. 161907-1 -161907-3, 2007.

[13] K. Hu, Z. H. Cao, and X. K. Meng, "Inverse effect of thickness on the ductility in nanocrystalline Cu films," *Materials Science and Engineering: A,* vol. 528, no. 29-30, pp. 8546-8550, 2011.

[14] Z. H. Cao, K. Hu, and X. K. Meng, "Strain rate sensitive stretchability and fracture behavior of nanocrystalline Cu films on flexible substrate," *Materials Science and Engineering: A,* vol. 536, pp. 244-248, 2012.

[15] N. Lu, X. Wang, Z. Suo, and J. Vlassak, "Failure by simultaneous grain growth, strain localization, and interface debonding in metal films on polymer substrates," *Journal of Materials Research,* vol. 24, no. 2, pp. 379-385, 2009.

[16] J. R. Bautista, F. Avilés, A. I. Oliva, O. Ceh, and J. E. Corona, "Correlations between mechanical stress, electrical conductivity and nanostructure in Al films on a polymer substrate," *Materials Characterization,* vol. 61, no. 3, pp. 325-329, 2010.

[17] G.-D. Sim, S. Won, C.-y. Jin, I. Park, S.-B. Lee, and J. J. Vlassak, "Improving the stretchability of as-deposited Ag coatings on poly-ethylene-terephthalate substrates through use of an acrylic primer," *Journal of Applied Physics,* vol. 109, no. 7, pp. 073511-1 - 073511-5, 2011.

[18] K. L. Mei-yu Chen, Run-jun Sun, Hong-tian Fang, and Wei Liu, "Factors Affecting on the Electricity Properties of a Metal-PET Composite During Tensile Deformation," *Polymers & Polymer Composites,* vol. 23, no. 3, pp. 159-166, 2015.

[19] M. M. Hamasha, K. Alzoubi, J. C. Switzer, S. Lu, S. B. Desu, and M. Poliks, "A study on crack propagation and electrical resistance change of sputtered aluminum thin film on poly ethylene terephthalate substrate under stretching," *Thin Solid Films,* vol. 519, no. 22, pp. 7918-7924, 2011.

[20] N. Lu, X. Wang, Z. Suo, and J. Vlassak, "Metal films on polymer substrates stretched beyond 50%," *Applied Physics Letters,* vol. 91, no. 22, pp. 221909-1 - 221909-3, 2007.

[21] !!! INVALID CITATION !!! [21].

[22] Y.-S. Lee, G.-D. Sim, J.-S. Bae, J.-Y. Kim, and S.-B. Lee, "Tensile and fatigue behavior of polymer supported silver thin films at elevated temperatures," *Materials Letters,* vol. 193, pp. 81-84, 2017.

[23] T. R. Hull, J. S. Colligon, and A. E. Hill, "Measurement of thin film adhesion," *Vacuum,* vol. 37, no. 4, pp. 327-330, 1987.

[24] M. Jesdinszki, C. Struller, N. Rodler, D. Blondin, V. Cassio, E. Kucukpinar, and H.-C. Langowski, "Evaluation of Adhesion Strength Between Thin Aluminum Layer and Poly(ethylene terephthalate) Substrate by Peel Tests — A Practical Approach for the

Packaging Industry," *Journal of Adhesion Science and Technology,* vol. ahead-of-print, no. ahead-of-print, pp. 1-24, 2012.

[25] J. Wang, R. L. Weaver, and N. R. Sottos, "A parametric study of laser induced thin film spallation," *Experimental Mechanics,* vol. 42, no. 1, pp. 74-83, 2002.

[26] L. Hu, J. Wang, Z. Li, S. Li, and Y. Yan, "Interfacial adhesion of nanoporous zeolite thin films," *Journal of Materials Research,* vol. 21, no. 2, pp. 505-511, 2006.

[27] S. S. V. Kandula, C. D. Hartfield, P. H. Geubelle, and N. R. Sottos, "Adhesion strength measurement of polymer dielectric interfaces using laser spallation technique," *Thin Solid Films,* vol. 516, no. 21, pp. 7627-7635, 2008.

[28] R. Ecault, F. Touchard, M. Boustie, L. Berthe, and N. Dominguez, "Numerical modeling of laser-induced shock experiments for the development of the adhesion test for bonded composite materials," *Composite Structures,* vol. 152, pp. 382-394, 2016.

[29] N. Inagaki, S. Tasaka, K. Narushima, and H. Kobayashi, "Surface modification of PET films by pulsed argon plasma," *Journal of Applied Polymer Science,* vol. 85, no. 14, pp. 2845-2852, 2002.

[30] S. M. Pelagade, N. L. Singh, A. Qureshi, R. S. Rane, S. Mukherjee, U. P. Deshpande, V. Ganesan, and T. Shripathi, "Investigation of surface properties of Ar-plasma treated polyethylene terephthalate (PET) films," *Nuclear Instruments and Methods in Physics Research Section B: Beam Interactions with Materials and Atoms,* vol. 289, pp. 34-38, 2012.

[31] N. Inagaki, S. Tasaka, and S. Shimada, "Comparative studies on surface modification of poly(ethylene terephthalate) by remote and direct argon plasmas," *Journal of Applied Polymer Science,* vol. 79, pp. 808-815, 2001.

[32] J. Hyun, P. Barletta, K. Koh, S. Yoo, J. Oh, D. E. Aspnes, and J. J. Cuomo, "Effect of Ar + ion beam in the process of plasma surface modification of PET films," *Journal of Applied Polymer Science,* vol. 77, pp. 1679-1683, 2000.

[33] I. A. Rusu, G. Popa, S. O. Saied, and J. L. Sullivan, "Ar rf plasma treatment of PET films for Si films adhesion improvement," *Journal of Optoelectronics and Advanced Materials,* vol. 8, no. 5, pp. 1935-1938, 2006.

[34] G. Garnier, B. Chehab, B. Yrieix, Y. Bréchet, and L. Flandin, "On the essential work of fracture in polymer–metal multilayers," *Journal of Materials Science,* vol. 44, no. 20, pp. 5537-5543, 2009.

[35] L. M. Barker, and R. E. Hollenbach, "Shock-Wave Studies of PMMA, Fused Silica, and Sapphire," *Journal of Applied Physics,* vol. 41, no. 10, pp. 4208-4226, 1970.

[36] John R. Rumble, CRC Handbook of Chemistry and Physics, 101st Edition (Internet Version

2020), CRC Press/Taylor & Francis, Boca Raton, FL.

[37] J. Wang, R. L. Weaver, and N. R. Sottos, “Laser-induced decompression shock development in fused silica,” *Journal of Applied Physics,* vol. 93, no. 12, pp. 9529-9536, 2003.

[38] M. Bou, J.M. Martin, and T. L. Mogne, “Chemistry of the interface between aluminium,” *Applied Surface Science,* vol. 47, pp. 149-161, 1991.

[39] M. R. Begley, and H. Bart-Smith, “The electro-mechanical response of highly compliant substrates and thin stiff films with periodic cracks,” *International Journal of Solids and Structures,* vol. 42, no. 18-19, pp. 5259-5273, 2005.

[40] B. E. Alaca, M. T. A. Saif, and H. Sehitoglu, “On the interface debond at the edge of a thin film on a thick substrate,” *Acta Materialia,* vol. 50, pp. 1197-1209, 2002.

[41] M. R. Begley, O. N. Scott, M. Utz, and H. Bart-Smith, “Fracture of nanoscale copper films on elastomer substrates,” *Applied Physics Letters,* vol. 95, no. 23, pp. 231914-1 - 231914-3, 2009.